Geosci. Model Dev., 19, 4725–4747, 2026
https://doi.org/10.5194/gmd-19-4725-2026

Geoscientific Model Development
Open Access
EGU

Process-based evaluation of ENSO simulation sensitivity to horizontal resolution in the Chinese Academy of Sciences FGOALS-f3 Climate System Model

Meng-Er Song[1], Lin Chen[1], Yongqiang Yu[2], Bo An[2], Jiuwei Zhao[1], and Hai Zhi[1]

[1]State Key Laboratory of Climate System Prediction and Risk Management/Key Laboratory of Meteorological Disaster, Ministry of Education/Collaborative Innovation Center on Forecast and Evaluation of Meteorological Disasters, Nanjing University of Information Science and Technology, Nanjing 210044, China
[2]State Key Laboratory of Earth System Numerical Modeling and Application, Institute of Atmospheric Physics, Chinese Academy of Sciences, Beijing, China

Correspondence: Lin Chen (chenlin@nuist.edu.cn)

Received: 3 December 2025 – Discussion started: 21 January 2026
Revised: 15 April 2026 – Accepted: 1 May 2026 – Published: 2 June 2026

Abstract. The El Niño–Southern Oscillation (ENSO) is the most prominent mode of interannual climate variability; its simulation performance represents a critical benchmark for evaluating the fidelity of coupled climate models. Increasing model resolution is an effective approach to improve the climate model performance; however, the impact of refining horizontal resolution from the hundred-kilometer scale to the tens-of-kilometer scale on ENSO simulation, as well as the underlying mechanisms, remains unclear. This study provides a process-based evaluation of ENSO behavior in two versions of the Chinese Academy of Sciences Flexible Global Ocean–Atmosphere–Land System Finite-Volume version 3 (FGOALS-f3) climate system model: a low-resolution configuration (∼ 100 km; FGOALS-f3-L, hereafter f3-L) and a high-resolution configuration (∼ 25 km; FGOALS-f3-H, hereafter f3-H). Using a reproducible diagnostic framework, we assess how horizontal resolution influences ENSO amplitude, oscillation irregularity, key air–sea coupling processes, and high-frequency (HF) atmospheric variability. The low-resolution version severely overestimates ENSO amplitude, whereas f3-H produces amplitude closer to the observation. Process-based diagnostics show that this improvement arises from the more realistic representation of thermocline and zonal advection feedback processes in f3-H, which arises from the more realistic representation of the meridional structure of ENSO-related zonal wind stress anomalies over equatorial Pacific in f3-H and can be traced back to its improved horizontal resolution. The ENSO cycle in f3-L exhibits excessive regularity, featuring periodic warm-cold transitions; while f3-H reproduces an irregular oscillation resembling the observation. The excessive regularity in f3-L is attributed to its coarser resolution, which limits the simulation performance of tropical cyclones and consequently weakens high-frequency westerly wind activity over the tropical Pacific. The weak stochastic forcing in f3-L is insufficient to disrupt its overly intense ENSO cycle, yielding an overly regular oscillation. By identifying the structural sources of ENSO biases across resolutions, this study provides a reproducible and model-agnostic framework for diagnosing resolution effects on ENSO performance in climate models and informs future development of the FGOALS model family.

1 Introduction

El Niño–Southern Oscillation (ENSO), as one of the most prominent interannual variabilities in the Earth's climate system, exerts a profound influence on regional and global climate (McPhaden et al., 2006; Cai et al., 2021). Therefore, the ability to accurately simulate ENSO phenomenon serves as a fundamental benchmark for evaluating the fidelity of coupled climate models (Timmermann et al., 2018). Despite significant progress in the development of climate models, large

inter-model spread remains in ENSO characteristics across Coupled Model Intercomparison Project (CMIP) generations (Zhang et al., 2020; Planton et al., 2021). Common biases include inaccuracies in simulating ENSO amplitude (Planton et al., 2021), period (Lu et al., 2018), seasonal phase locking (Liao et al., 2023; Yan and Sun, 2024), spatial distribution (Jiang et al., 2021), and intensity asymmetry (Zhao and Sun, 2022), as well as an overly regular ENSO oscillation (Chen et al., 2016a; Guilyardi et al., 2020). These deficiencies reflect systematic structural biases within models, which directly limit the predictive skill of dynamical models (Barnston et al., 2012) and hinder the reliability of climate projection regarding how ENSO may evolve under future climate change (Jiang et al., 2020a). Therefore, it is imperative to improve the fidelity of ENSO simulation in climate models.

Horizontal resolution has long been recognized as an important factor influencing model behavior (Yu et al., 2024). Motivated by this, the latest CMIP6 launched a dedicated High-Resolution Model Inter-comparison Project (HighResMIP) (Eyring et al., 2016) to systematically assess the benefits of increased resolution on model simulations. Previous studies have shown that as model resolution increases, simulation capabilities for both the climate mean state and variability exhibit improvements (Dawson et al., 2013; Chang et al., 2020). For example, high-resolution models demonstrate superior performance over low-resolution counterparts in simulating the Asian summer monsoon (He et al., 2025a), the impact of Tibetan Plateau thermal forcing on Asian summer monsoon (He et al., 2025b), the precipitation in southern China (Zi et al., 2024), the spatial distribution and frequency of tropical cyclones (Kreussler et al., 2021; Li et al., 2021), air–sea turbulent flux (Small et al., 2019), heat transport by boundary currents (Docquier et al., 2019), ocean mesoscale eddies (Hallberg, 2013), and Antarctic sea ice (Docquier et al., 2019). This is partly because higher resolution allows models to explicitly resolve finer-scale physical processes, reducing their dependence on parameterization schemes. Furthermore, high-resolution models facilitate a more accurate simulation of topographically sensitive regions, therefore improving the simulation of atmosphere-ocean processes related to complex terrain (Bacmeister et al., 2014; Hewitt et al., 2016). Then a pertinent inquiry arises: does the ENSO simulation benefit from the increased resolution?

Regarding the impact of increased horizontal resolution on ENSO characteristics, previous studies found that when the atmospheric horizontal resolution in climate models was increased from 3.8° (T30) or 2.8° (T42) to 1° (T106), significant improvements can be found in the simulated ENSO period (Guilyardi et al., 2004; Navarra et al., 2008) and ENSO amplitude (Hua et al., 2018). However, the aforementioned studies were primarily based on the comparisons from $\sim$ 400 km (or 300 km) to 100 km scales. In the latest climate models participated in the HighResMIP, model resolutions have advanced substantially, with some achieving 25 km resolution in atmospheric component and 10 km in oceanic component. This higher resolution enables a more realistic reproduction of climate variability, such as tropical cyclones (TCs) (Li et al., 2021) and tropical instability waves (Li et al., 2023). Yet, a critical question remains unresolved: when model resolution reaches $\sim$ 25 km, a scale that can reasonably simulate weather-scale systems like TCs, does ENSO simulation also improve further?

ENSO is fundamentally driven by a number of coupled ocean-atmosphere feedbacks (Li, 1997; Jin et al., 2006; Chen et al., 2015b, 2016a); however, some analyses regarding ENSO simulations are often result-oriented, focusing only on changes in statistical indices while lacking sufficient diagnostic analysis of the key air–sea feedback processes that shape ENSO's properties. Therefore, it is necessary to conduct a process-oriented evaluation when comparing the ENSO simulation between different resolution versions.

It is worth noting that the observational evidences have suggested the significant influence of atmospheric "noise" on the development and evolution of ENSO (Chen et al., 2015a; Fedorov et al., 2015). Here the atmospheric "noise" primarily refers to high-frequency (HF) wind activities such as westerly wind bursts (Harrison and Vecchi, 1997; Fedorov, 2002), including synoptic and intra-seasonal scales. TC and Madden-Julian Oscillation (MJO; Madden and Julian, 1971; Madden and Julian, 1972) have been recognized as key sources of HF wind activities in recent studies (Ying et al., 2019; Liang and Fedorov, 2021). Considering the atmospheric components in HighResMIP models can reach a horizontal resolution of 50 km or finer (which is sufficient to reasonably reproduce TC features) and that the simulation performance for TC and MJO activities improves with increasing resolution (Davis, 2018; Tang et al., 2022; Roberts et al., 2025), a further question arises: does the improved simulation of HF activities like TCs and MJO in high-resolution models contribute to improved ENSO simulation?

Motivated by these open questions, this study will conduct a process-oriented evaluation of ENSO simulation for a Chinese climate model, the Flexible Global Ocean–Atmosphere–Land System Finite-Volume version 3 (FGOALS-f3) climate system model that was developed by the Institute of Atmospheric Physics, Chinese Academy of Sciences (IAP-CAS). FGOALS-f3 participated in HighResMIP with both a low-resolution ($\sim$ 100 km; FGOALS-f3-L, hereafter f3-L) and a high-resolution version ($\sim$ 25 km; FGOALS-f3-H, hereafter f3-H) (An et al., 2022; Bao et al., 2020). The high-resolution version (f3-H) has been shown to have superior simulation performances over the low-resolution counterpart (f3-L) in representing mesoscale vortices (An et al., 2022), tropical instability waves (Li et al., 2023), TCs (Li et al., 2021), East Asian summer monsoon precipitation (Zi et al., 2024), and the climatological mean states (Yu et al., 2024). Therefore, this study employs the CAS-developed f3-H and f3-L to

reveal the impact of model resolution on ENSO simulation performance and the underlying air–sea coupling processes.

This model evaluation study will provide insights into the resolution sensitivity of ENSO-related processes in FGOALS-f3 and establishes a diagnostic framework that can be applied to other coupled models participating in CMIP6 and future CMIP phases. The remainder of this paper is organized as follows. Section 2 describes the model configurations, observational datasets, and diagnostic framework. Section 3 presents an overview of the ENSO characteristics in two versions of FGOALS-f3 model. Sections 4 and 5 demonstrate how the model horizontal resolution impacts the ENSO simulation. Section 6 summarizes the findings and discusses implications for model development and evaluation.

2 Model configurations, datasets, and diagnostic framework

2.1 Model configurations

FGOALS-f3 is a fully coupled climate system model developed by State Key Laboratory of Numerical Modeling for Atmospheric Sciences and Geophysical Fluid Dynamics (LASG), IAP-CAS, which couples four component models using the CPL7 coupler (Craig et al., 2012). The four component models are the atmospheric model FAMIL2.2 (He et al., 2019; Li et al., 2021), the ocean model LICOM3.0 (Li et al., 2020), the land model CLM4.0 (Lawrence et al., 2011), and the sea ice model CICE4.0 (Hunke and Lipscomb, 2010).

The atmospheric component FAMIL2.2 is the last version of the Finite-volume Atmospheric Model developed by the LASG-IAP (FAMIL) (Li et al., 2021). FAMIL2.2 utilizes a finite-volume dynamical core constructed on a cubed sphere grid that is globally partitioned into six tiles (Zhou et al., 2015). In the vertical direction, the model uses hybrid coordinates over 32 layers, and the model top is 1 hPa. While the horizontal resolution ranges from C96 (about 100 km) to C384 (about 25 km) across the different resolution version. The oceanic component LICOM 3.0 is the third version of LASG-IAP Climate System Ocean Model (LICOM) (Yu et al., 2018). LICOM 3.0 updated a new advection scheme and employed a tripolar grid based on orthogonal curvilinear coordinates. The horizontal resolution of LICOM 3.0 can vary flexibly between 1 and 1/20°. Subgrid parametrization schemes employed in LICOM 3.0 include the tidal mixing scheme, a buoyancy frequency related thickness diffusivity scheme, a vertical viscosity and diffusion scheme, and a chlorophyll *a* dependent solar penetration scheme, etc. A comprehensive description of the physical package in LICOM 3.0 can be found in Li et al. (2020). The land component in FGOALS-f3 model is Community Land Model (CLM) version 4.0. This advanced model simulates the water and momentum balances at the land surface and incorporates interactive carbon and nitrogen cycles, allowing for a more realistic representation of vegetation dynamics and ecosystem processes (Lawrence et al., 2011). In FGOALS-f3 model, sea ice is simulated using the Los Alamos Sea Ice Model version 4.0 (CICE 4.0). This is a dynamic-thermodynamic model that simulates the evolution of sea ice thickness, concentration, and velocity. It features multiple ice thickness categories and an elastic-viscous-plastic (EVP) rheology to model ice deformation and dynamics (Hunke and Lipscomb, 2010).

The FGOALS-f3 model includes two versions: f3-L and f3-H (He et al., 2019; An et al., 2022). Both models are participating in HighResMIP of CMIP6 and have successfully completed the Tier-1 and Tier-3 experiments. These two models have the same components and physical processes. The sole distinction between f3-H and f3-L lies in their horizontal resolution and the corresponding time steps within their finite-volume cubed-sphere dynamical core (FV3). To maintain the stability of the integration for the dynamical core, the two parameters (k_split and n_split) in FV3 are set to 6 and 15 in f3-H, respectively (they are 2 and 6, respectively, in f3-L). The specific resolutions of each component of f3-L and f3-H models are shown in Table 1.

The model data used in this study are obtained from the historical experiment outputs of f3-L and f3-H model. Considering the experiment outputs of f3-H (highresSST-present) start from 1950, the period during 1950–2014 for the two models are analyzed. The main variables used in this study include monthly sea surface temperature (SST), three-dimensional ocean currents (uo, vo, wo), oceanic potential temperature (thetao), surface wind stress (tauu, tauv), and net radiation flux (rsds, rsus, rlds, rlus, hfss, hfls); daily surface wind (uas, vas), precipitation (pr), six-hourly sea level pressure (SLP), 850 hPa wind (ua, va), 300 and 500 hPa temperature (ta). All data is detrended before analyzing.

2.2 Observation and reanalysis datasets

The observational and reanalysis data used in this study include: (1) the monthly SST data obtained from the Hadley Centre Sea Ice and Sea Surface Temperature version 1.1 dataset (HadISST v1,1), with a horizontal resolution of $1° \times 1°$ (Rayner et al., 2003); (2) the monthly, daily, and hourly 10m wind fields are from the European Centre for Medium-Range Weather Forecasts (ECMWF) reanalysis data Fifth Generation (ERA5), with a horizontal resolution of $0.25° \times 0.25°$ (Hersbach et al., 2020); (3) the daily precipitation is from the Global Precipitation Climate Program version 1.3 (GPCP v1.3), with a horizontal resolution of $2.5° \times 2.5°$ (Adler et al., 2003); (4) the monthly sea surface wind stress data are provided by the ECMWF Ocean Reanalysis Data (ORAS5), with a horizontal resolution of $1° \times 1°$ (Zuo et al., 2019) and America Ocean Data Assimilation Data Set version 2.2.4 (SODA v2.2.4), with a horizontal resolution of $0.5° \times 0.5°$ (Carton and Giese, 2008); (5) the

Table 1. Resolution comparison of each component model between the FGOALS-f3-L model and the FGOALS-f3-H model.

	FGOALS-f3-L	FGOALS-f3-H
Atmosphere	FAMIL2.2 (1° × 1°, 32 levels)	FAMIL2.2 (0.25° × 0.25°, 32 levels)
Ocean	LICOM3.0 (1° × 1°, 30 levels)	LICOM3.0 (0.1° × 0.1°, 55 levels)
Land	CLM4.0 (1.25° × 0.9°)	CLM4.0 (0.31° × 0.23°)
Sea Ice	CICE4.0 (1° × 1°)	CICE4.0 (0.1° × 0.1°)

historical TC data are from the China Meteorological Administration (CMA) tropical cyclone best track dataset (Ying et al., 2014; Lu et al., 2021).

2.3 Diagnostic framework

This study employs a reproducible, model-agnostic diagnostic framework for evaluating resolution-dependent ENSO behavior. Diagnostics include ENSO amplitude and spectrum, ENSO irregularity index, Bjerknes index diagnosis and the corresponding total derivative decomposition, meridional distribution index of zonal wind stress anomaly, oceanic zonal current decomposition, the HF atmospheric westerly (easterly) wind index and the corresponding noise-to-signal ratio, and TC detection and metrics.

Throughout this study, an overbar $\overline{()}$ denotes the climatological mean field, and a prime $()'$ denotes the interannual anomaly obtained by removing the climatological seasonal cycle. The subscript "HF" indicates a HF (sub-90 d) filtered field. For example, u'_{HF} denotes the HF component of daily zonal wind anomaly, obtained by applying a 90 d high-pass filter to the daily anomaly field. All symbols are used consistently throughout the paper unless otherwise specified.

2.3.1 ENSO amplitude, spectral analysis and ENSO irregularity index

Monthly SST anomaly (SSTA) is computed after removing the climatological seasonal cycle. ENSO amplitude is measured by the standard deviation of Niño3.4 index (monthly SSTA averaged in 5° S–5° N, 170–120° W). Power spectra are derived using the multi-taper method following Thomson (1982). To quantitatively evaluate the regularity of ENSO oscillation, we propose an ENSO irregularity index based on the coefficient of variation of inter-event time intervals (CVT). This metric is computed through the following steps.

First, ENSO events are identified using the 3-month running mean of the Niño3.4 index. A warm (cold) event is defined when the 3-month running mean Niño3.4 index exceeds 0.5 (falls below −0.5) standard deviation of the Niño3.4 index, and the event is considered to terminate when the Niño3.4 index returns to within the ±0.5 standard deviation range for at least two consecutive months.

Second, the time interval between two successive events of the same sign is defined as the time separation between adjacent event peaks (i.e., the month of maximum warming for warm events or maximum cooling for cold events).

Third, the CVT is computed as the ratio of the standard deviation to the mean of these inter-event intervals:

$$\mathrm{CVT} = \frac{\sigma_T}{\mu_T} \tag{1}$$

where T denotes the set of all inter-event intervals, and μ_T and σ_T denote the mean and the standard deviation of these intervals, respectively.

Finally, the CVT is calculate separately for warm events ($\mathrm{CVT_{warm}}$) and cold events ($\mathrm{CVT_{cold}}$), and their average is taken as the final ENSO irregularity index used in this study. A larger CVT indicates more irregular ENSO oscillation with highly variable inter-event spacing, whereas a smaller CVT (approaching zero) indicates a more periodic and regular oscillation.

2.3.2 Bjerknes index diagnosis

In order to quantitatively analyze the air–sea coupling processes responsible for ENSO amplitude in FGOALS-f3 models, the diagnostic framework of BJ index (Kim and Jin, 2011a, b) is performed in this study. The specific formulation is listed as follows:

$$\mathrm{BJ} = \frac{R-\varepsilon}{2} \tag{2}$$

$$R = -\left(a_1\frac{\langle\Delta\overline{u}\rangle_{\mathrm{E}}}{L_x} + a_2\frac{\langle\Delta\overline{v}\rangle_{\mathrm{E}}}{L_y}\right) - \alpha_{\mathrm{s}} + \mu_{\mathrm{a}}\beta_{\mathrm{u}}\left\langle -\frac{\partial\overline{T}}{\partial x}\right\rangle_{\mathrm{E}} + \mu_{\mathrm{a}}\beta_{\mathrm{w}}\left\langle -\frac{\partial\overline{T}}{\partial z}\right\rangle_{\mathrm{E}} + \mu_{\mathrm{a}}\beta_{\mathrm{h}}a_{\mathrm{h}}\left\langle\frac{\overline{w}}{H_1}\right\rangle_{\mathrm{E}} \tag{3}$$

$$\frac{\partial\langle h'\rangle_{\mathrm{W}}}{\partial t} = -\varepsilon\langle h'\rangle_{\mathrm{W}} - F\left[\tau'_x\right] \tag{4}$$

$$\left\langle Q'\right\rangle_{\mathrm{E}} = -\alpha_{\mathrm{s}}\left\langle T'\right\rangle_{\mathrm{E}} \tag{5}$$

$$\left\langle H(\overline{w})T'_{\mathrm{sub}}\right\rangle_{\mathrm{E}} = a_{\mathrm{h}}\left\langle T'\right\rangle_{\mathrm{E}} \tag{6}$$

$$\left\langle h'\right\rangle_{\mathrm{E}} - \left\langle h'\right\rangle_{\mathrm{W}} = \beta_{\mathrm{h}}\left[\tau'_x\right] \tag{7}$$

$$\left\langle H(\overline{w})w'\right\rangle_{\mathrm{E}} = \beta_{\mathrm{w}}\left[\tau'_x\right] \tag{8}$$

$$\left\langle u'\right\rangle_{\mathrm{E}} = \beta_{\mathrm{u}}\left[\tau'_x\right] + \beta_{\mathrm{u}h}\left\langle h'\right\rangle_{\mathrm{W}} \tag{9}$$

$$\left[\tau'_x\right] = \mu_{\mathrm{a}}\left\langle T'\right\rangle_{\mathrm{E}} \tag{10}$$

where u, v, and w are the three dimensional oceanic current velocity; T denotes sea surface temperature (°C); $\langle\rangle_{\mathrm{E}}$ and $\langle\rangle_{\mathrm{W}}$ represent averaged volume of the eastern box region

(5° S–5° N, 170–90° W) and western box region (5° S–5° N, 130° E–170° W), respectively, from the ocean surface to the mixed layer depth; L_x and L_y denote the longitudinal and latitudinal lengths of the eastern box, respectively; H_1 denotes the mixed layer depth (two complementary strategies for specifying H_1 are adopted in this study and their results are compared in Sect. 4.1). The coefficients a_1 and a_2 are obtained through linear regression using SSTA zonally or meridionally averaged at the boundaries and area-averaged SSTA over the box. The "Δ" in Eq. (2) represents the differences of ocean current between the eastern and western boundaries. $H(\overline{w}) = \begin{cases} 1, & \overline{w} > 0 \\ 0, & \overline{w} \le 0 \end{cases}$ is the step function to make sure only upward vertical motion is taken into account. Here, the Eq. (1) defines the BJ index, serving as the primary metric for the growth rate examined in this analysis. The corresponding dynamic and thermodynamic feedbacks are expressed in Eq. (2). In Eq. (3), the first term on the right-hand side is the damping process at the rate of ε; the second term represents the Sverdrup transport across the equatorial Pacific basin. In Eqs. (4) to (9), α_s (s^{-1}) indicates the response of the thermodynamic damping to SSTA; μ_a ($N\,m^{-2}\,K^{-1}$) represents the response of surface wind stress anomalies (τ_x') to SSTA; β_u ($m\,s^{-1}\,(N\,m^{-2})^{-1}$) represents the response of upper ocean current anomalies (u_o') to τ_x'; β_h ($m\,(N\,m^{-2})^{-1}$) indicates the response of the anomalous zonal slope of the equatorial Pacific thermocline to τ_x'; β_w ($m\,s^{-1}\,(N\,m^{-2})^{-1}$) denotes the response of ocean upwelling anomalies (w_o') to τ_x'; a_h ($K\,m^{-1}$) shows the effect of thermocline depth change on subsurface temperature anomalies.

Based on the above equations, the main contributing terms of the BJ index include two negative feedback processes: the dynamic damping by mean advection (MA; $-\left(a_1\frac{\langle\Delta\overline{u}\rangle_E}{L_x}+a_2\frac{\langle\Delta\overline{v}\rangle_E}{L_y}\right)$), the thermodynamic feedback (TD; $-\alpha_s$), and three positive feedback processes: the zonal advection feedback (ZA; $\mu_a\beta_u\langle-\frac{\partial\overline{T}}{\partial x}\rangle_E$), the thermocline feedback (TH; $\mu_a\beta_h a_h\langle\frac{\overline{w}}{H_1}\rangle_E$), and the Ekman feedback (EK; $\mu_a\beta_w\langle-\frac{\partial\overline{T}}{\partial z}\rangle_E$).

2.3.3 Meridional distribution index

To further quantify the meridional structure of ENSO-related τ_x', a meridional distribution index (MDI) that was proposed by Chen et al. (2015b), is employed. The MDI is defined as:

$$\mathrm{MDI} = \frac{\int_{-10^\circ}^{10^\circ}\tau_x'(y)\,|y|\,\mathrm{d}y}{\int_{-10^\circ}^{10^\circ}\tau_x'(y)\mathrm{d}y} \tag{11}$$

where y denotes latitude, and $\tau_x'(y)$ represents the meridional profile of the normalized τ_x'. The normalized τ_x' obtained by regressing the zonal wind stress anomaly field onto the Niño4 region (5° S–5° N, 160° E–150° W) averaged zonal wind stress anomalies and then averaged over the Niño4 longitude range (160° E–150° W). The MDI provides a quantitative measure of the meridional concentration of ENSO-related τ_x' within the equatorial band. Specifically, a smaller MDI indicates that τ_x' is more concentrated near the equator, whereas a larger MDI indicates a broader meridional distribution.

2.3.4 Oceanic zonal current decomposition

ENSO-related zonal current anomaly (u_o') in the equatorial region is composed of anomalous zonal geostrophic currents (u_g') and anomalous Ekman currents (u_e') (Su et al., 2010; Su et al., 2014). The specific formulas of u_g' and u_e' are listed below:

$$u_g' = -\frac{g\partial^2 D'}{\beta\partial y^2} \tag{12}$$

$$u_e' = \frac{1}{\rho H_1}\frac{r_s\tau_x' + \beta y\tau_y'}{r_s^2 + (\beta y)^2} \tag{13}$$

where β and r_s are the planetary vorticity gradient and Rayleigh dissipation rate ($0.5\,d^{-1}$), respectively; τ_y' denotes the sea meridional wind stress anomaly; H_1 denotes the mean mixed layer depth, and ρ is the seawater density.

2.3.5 HF westerly (easterly) wind index and noise-to-signal ratio

An index regarding the HF zonal wind anomalies is used to quantitatively measure the intensity of HF westerly (easterly) wind activity in the f3-L and f3-H models. This index (named WWI index and EWI index) is defined as the integration of the averaged zonal HF westerly (easterly) wind over a fixed region (5° S–5° N, 120–180° E). The formula is as follows:

$$\text{WWI index} = \int_{\text{time1}}^{\text{time2}} u_{HF}'\mathrm{d}t,\ u_{HF}' > 1\,m\,s^{-1} \tag{14}$$

$$\text{EWI index} = \int_{\text{time1}}^{\text{time2}} u_{HF}'\mathrm{d}t,\ u_{HF}' < -1\,m\,s^{-1} \tag{15}$$

where u_{HF}' represents the daily zonal wind anomaly after applying a 90 d high-pass filter, time1 and time2 represent the start and end time of the integrated period, respectively. In this study, the development period of ENSO event (January to August) is selected as the integrated period.

A noise-to-signal ratio (NSR) metric is proposed to quantify the relative magnitude of stochastic atmospheric forcing compared to the ENSO signal. The NSR is defined as:

$$\mathrm{NSR} = \frac{\sigma\left(u'_{\mathrm{HF}}\right)}{\sigma\left(\mathrm{SSTA}_{\mathrm{Niño3.4}}\right)} \tag{16}$$

where $\sigma(u'_{\mathrm{HF}})$ is the standard deviation of 90 d high-pass-filtered zonal wind anomalies averaged over the western equatorial Pacific (5° S–5° N, 120–180° E), and $\sigma(\mathrm{SSTA}_{\mathrm{Niño3.4}})$ denotes the standard deviation of Niño3.4 index. A larger NSR indicates stronger stochastic forcing relative to the ENSO signal, and vice versa.

2.3.6 TC detection and metrics

The TC detection algorithm developed by the Geophysical Fluid Dynamics Laboratory (https://www.gfdl.noaa.gov/tstorms/, last access: 28 May 2026; Zhao et al., 2023) was used to detect TC activities in FGOALS-f3 model. The basic identification criteria and steps are: (1) a local minimum SLP is found within a maximum distance of 3000 km; (2) the wind speed at 850 hPa for this vortex exceed 17 m s^{-1}; (3) the absolute value of the vorticity is greater than 1.5×10^{-4} s^{-1}; (4) the temperature within 1200 km of the vortex center is higher than that in the 1200–2400 km radius at 300–500 hPa, indicating a warm core structure; (5) the lifespan of this TC should be at least 3 d (72 h).

We further employ two metrics, i.e, accumulated cyclone energy (ACE) and TC track density (TCTD), to assess the TC activity in FGOALS-f3 models. The ACE index (Bell et al., 2000) in each grid cell is defined as the sum of the squares of the maximum surface wind speeds for all TCs occurring within a $4° \times 4°$ grid cell over all 6-hourly periods (i.e., $\mathrm{ACE} = \sum_i V_{\mathrm{max}}^2$, where i denotes the ith TC in a grid cell and V_{max} denotes its maximum surface wind speed). The TCTD in each grid is defined as the sum of the number of TCs that have passed through the region within a distance of $4° \times 4°$ from the grid center.

3 Evaluation of ENSO Characteristics in f3-L and f3-H

Figure 1 shows the spatial distribution of the standard deviation (SD) of SSTA over the tropical Pacific. In both the high- and low-resolution versions of FGOALS-f3, the interannual variability of SSTA is concentrated in the central-eastern equatorial Pacific (Fig. 1b and c), which is spatially consistent with the observation (Fig. 1a). However, significant differences exist in the ENSO amplitude. Specifically, the SD of the Niño3.4 index is 0.79° in the observation, 1.53° in f3-L, and 0.62° in f3-H, respectively. This indicates that f3-L severely overestimates the ENSO amplitude, whereas f3-H's simulation is much closer to the observation. Considering that the ENSO amplitude simulated in f3-L is approximately 2.5 times that of f3-H, this study will firstly address the causes of the stronger ENSO amplitude in f3-L compared to its counterpart in f3-H.

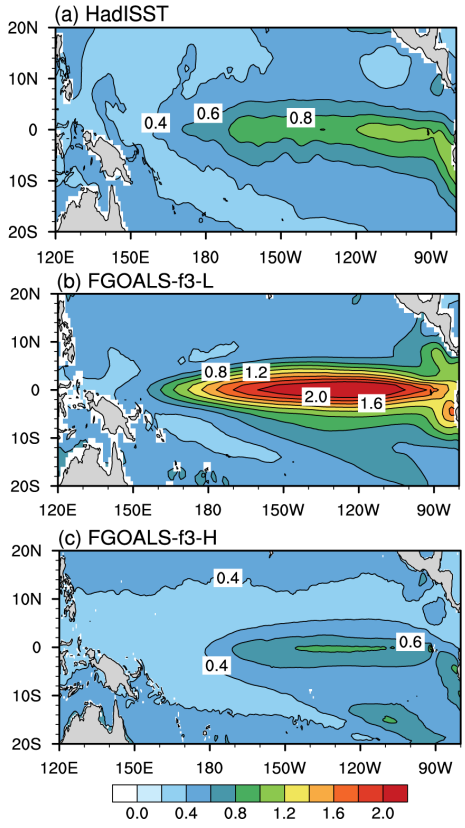

Figure 1. The standard deviation of SSTA (shading, units: °C) for **(a)** observation (HadISST), **(b)** f3-L and **(c)** f3-H.

Figure 2 presents the time series of the Niño3.4 index for the observation and the two model versions. Obviously, the oscillation intensity of Niño3.4 index in f3-L is much stronger than that in the observation and f3-H, consistent with the results of the SD analysis (Fig. 1). Another notable difference lies in the regularity of the oscillation: ENSO events in f3-L exhibit highly periodic behavior, with a regular transition between warm and cold phases. In contrast, the ENSO evolution in both the observation and f3-H exhibit obvious irregularity. Furthermore, we conduct the power spectrum analysis on the Niño3.4 indices (Fig. 3). In the observation, the power spectrum is characterized by a broad band of 2–8 years. However, the power spectrum in f3-L shows a sharp and significant unimodal peak at approximately 3-year period, with excessive concentration of ENSO energy at this dominant period. In contrast, f3-H reproduces a broadband spectral distribution similar to the observation.

Based on the proposed ENSO irregularity index, we calculated the CVT for the observation, f3-L and f3-H. As shown in Table 2, the CVT values are 0.61, 0.17, and 0.53 for the observation, f3-L and f3-H, respectively. The results clearly indicate that ENSO oscillation in f3-L is excessively regular compared to the observation (CVT of 0.17 vs. 0.61), whereas f3-H produces a degree of irregularity much closes to the ob-

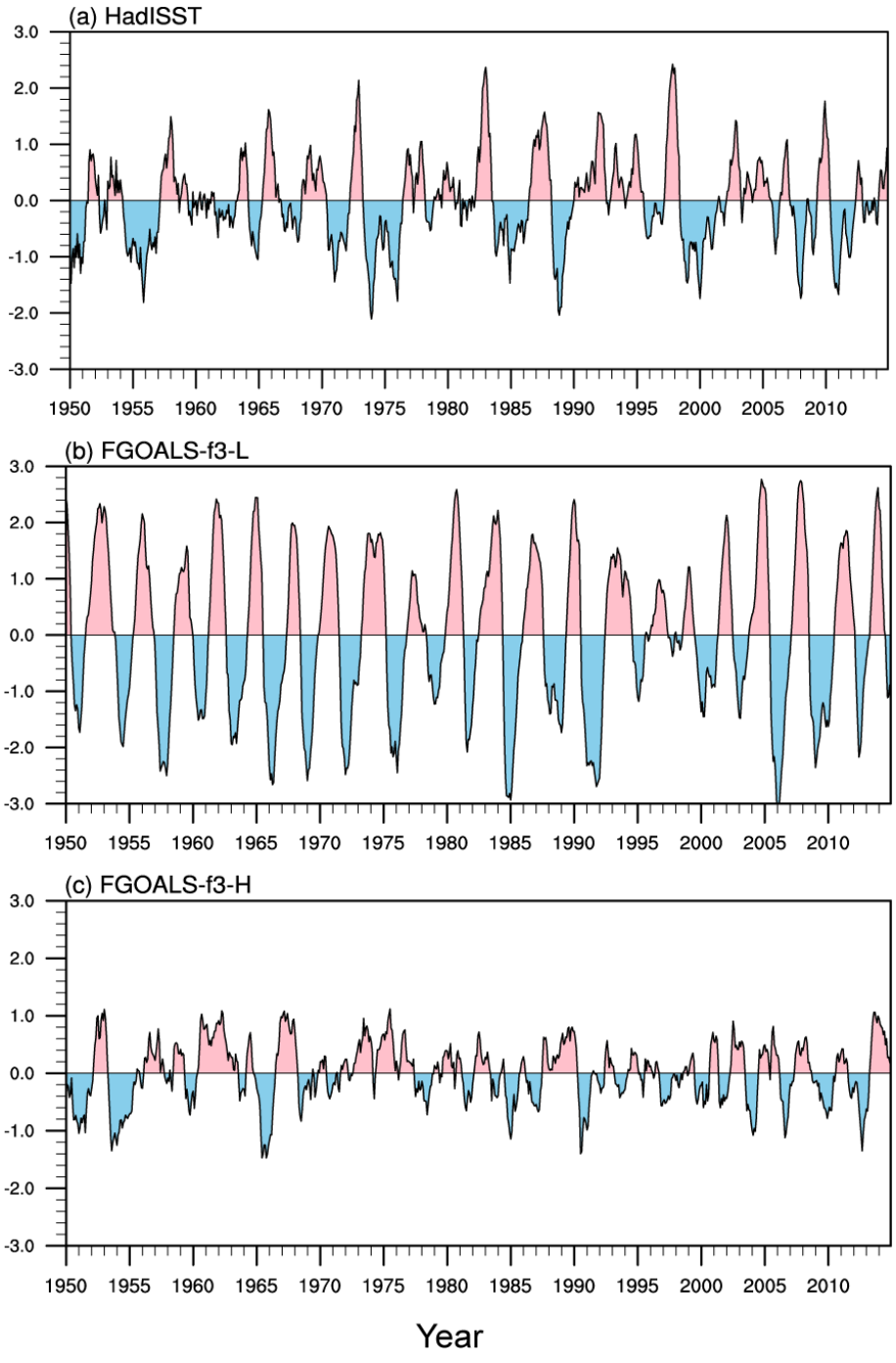

Figure 2. Temporal evolution of Niño3.4 index (the averaged SSTA in the Pacific Niño3.4 region (5° S–5° N, 170–120° W), units: °C) for **(a)** observation (HadISST), **(b)** f3-L and **(c)** f3-H.

servation. Therefore, the second question this study will address is: what causes the overly regular oscillation in f3-L, while f3-H captures more realistic irregularity?

4 Process-based diagnosis of ENSO amplitude differences

4.1 Diagnostic analysis based on the BJ index

To investigate the physical mechanisms responsible for the ENSO amplitude difference between the high- and low-

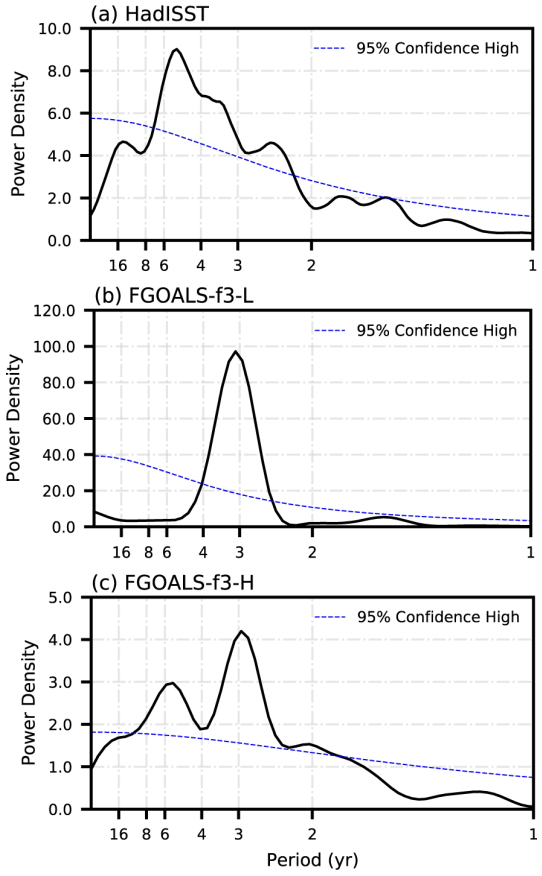

Figure 3. The power spectra of Niño3.4 index for **(a)** observation (HadISST), **(b)** f3-L and **(c)** f3-H. The blue line in the plots is the 95 % confidence level.

Table 2. The ENSO irregularity index (CVT) for the observation, f3-L and f3-H.

	Observation	f3-L	f3-H
CVT	0.61	0.17	0.53

resolution versions, we apply the BJ index framework to quantitatively diagnose the stability of the coupled ocean-atmosphere system in both models. When applying the BJ index or the commonly used mixed-layer heat budget diagnosis, one practical issue is the choice of mixed layer depth (MLD) and whether the results are sensitive to this choice. We therefore first examine the spatial distribution of the climatological MLD in f3-L and f3-H. Here the MLD is defined as the depth at which the ocean temperature is 0.8 °C lower than the SST, following Wang et al. (2012) and Chen et al. (2016b). As shown in Fig. S1 in the Supplement, the climatological MLD exhibits a pronounced zonal variation along the equatorial Pacific: it is relatively shallow in the far eastern Pacific and gradually deepens toward the central equatorial Pacific. Moreover, the MLD differs between the two model versions, with the eastern box-mean values of approximately 65 m in f3-L and 50 m in f3-H over the eastern equatorial Pacific (i.e., the eastern box used in the BJ index calculation). Given this zonal and inter-model variability, we adopt two complementary MLD strategies in the BJ index diagnostic.

Strategy 1 (Constant MLD): a fixed MLD of a constant value is applied to both f3-L and f3-H when computing the BJ index. This approach follows the conventional practice in previous BJ index studies (e.g., Kim and Jin, 2011a, b; Chen et al., 2019a, b) and facilitates a direct comparison between the two simulations under an identical diagnostic framework. From the perspective of the BJ-index eastern-box average, the climatological mean MLD over the eastern equatorial Pacific is approximately 65 m in f3-L and 50 m in f3-H. Therefore, in this first approach, we use a constant value of 65 m for both simulations.

The BJ index results under Strategy 1 are shown in Fig. 4. Figure 4 presents the BJ index calculated using a fixed MLD of 65 m for the reanalysis, f3-L and f3-H, as well as their difference (f3-L minus f3-H). The results demonstrate that, although both models yield negative BJ indices, the value for f3-L is significantly larger (i.e., less negative) than that for f3-H. According to the physical interpretation of the BJ index (Jin et al., 2006; Kim and Jin, 2011a, b), the less negative BJ index in f3-L indicates that the coupled air–sea system in f3-L is more unstable than that in f3-H. This more unstable coupled system is more favorable for ENSO growth, thereby leading to a stronger ENSO amplitude in f3-L than that in f3-H.

It is worth noting that the BJ index derived from the reanalysis is not more negative than that of f3-L, despite the observed ENSO amplitude being slightly weaker than that simulated by f3-L. This inconsistency can be attributed to two factors. First, reanalysis products carry inherent uncertainties, and direct comparison between reanalysis-derived and model-derived BJ indices should be interpreted with caution. Second, the BJ index is a linear diagnostic framework that does not account for nonlinear processes, including nonlinear atmospheric responses, semi-stochastic atmospheric noise (i.e., the HF zonal wind anomalies discussed in this study), and oceanic nonlinear processes such as nonlinear dynamical heating (Wei et al., 2026). In other words, while the BJ index is a useful tool for assessing whether the linear air–sea coupling framework favors ENSO growth, the actual ENSO amplitude is jointly determined by linear coupling, nonlinear processes, and stochastic forcing. This represents an inherent limitation of the BJ index framework. Therefore, a comprehensive evaluation of ENSO simulation requires not only the BJ index analysis of linear feedback processes but also diagnostics beyond the linear framework to assess the roles of nonlinear processes and stochastic forcing, as addressed in Sect. 5 of this study. In the following, our primary focus is on examining the differences in the BJ index and its contributing terms between f3-L and f3-H.

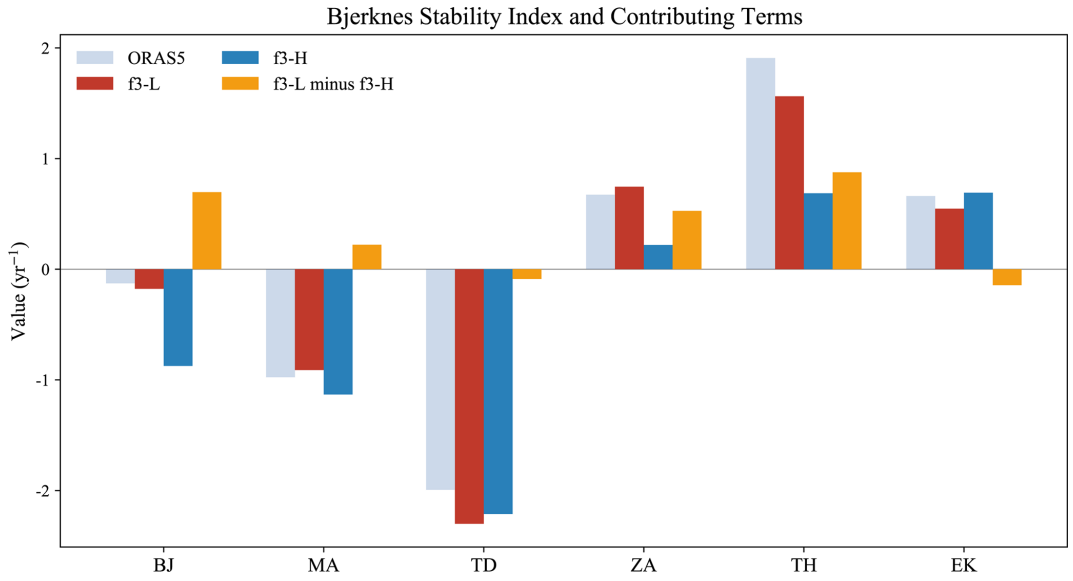

Figure 4. BJ index and the corresponding main contributing terms for the reanalysis (ORAS5; grey bars), f3-L (red bars), f3-H (blue bars) and their difference (f3-L minus f3-H, orange bars). Here the BJ index is calculated using a fixed MLD of 65 m. The five contributing terms include dynamic damping by mean advection (MA), thermodynamic damping feedback (TD), zonal advection feedback (ZA), thermocline feedback (TH) and Ekman feedback (EK).

A further question arises: which physical processes contribute to the more unstable coupled system in f3-L? By examining the differences in the five contributing terms of the BJ index (orange bars in Fig. 4), we find that the differences in the thermocline feedback (TH) term and the zonal advection feedback ZA) term are the dominant contributors to the BJ index difference (i.e., the system stability) between the two model versions. Therefore, the subsequent analysis will focus on the physical mechanisms responsible for the stronger TH and ZA terms in f3-L relative to f3-H.

Strategy 2 (Longitude-varying MLD): each model version uses its own longitude-dependent climatological MLD (averaged over the equatorial band, 5° S–5° N) when computing the BJ index. This approach accounts for zonal variations and inter-model differences in stratification, providing a more physically realistic diagnostic. In this approach, when calculating the BJ index, we diagnose the mixed-layer temperature anomaly above the longitudinally varying climatological MLD (Fig. S1) within the three-dimensional eastern equatorial Pacific box.

Figure S2 presents the BJ index and its contributing terms calculated using the longitude-varying MLD for the reanalysis, f3-L, and f3-H, as well as their difference (f3-L minus f3-H). The main results are broadly consistent with those obtained under Strategy 1. Specifically, the BJ index of f3-H remains more negative than that of f3-L, which largely explains the weaker ENSO amplitude in f3-H; and the BJ index difference between the two models is still primarily attributable to the TH and ZA terms. The only notable discrepancy between the two strategies lies in the MA term, which represents the dynamic damping by mean zonal and meridional advection. In brief, under the longitude-varying MLD strategy, the shallower MLD in f3-H means that the vertical averaging is taken over a thinner layer, in which the poleward (damping) branch dominates more strongly, resulting in a more negative MA term in f3-H compared to f3-L. A detailed analysis regarding the MA difference between f3-H and f3-L is provided in the Supplement (Sect. S1). Overall, the sensitivity test demonstrates that the core conclusions of the BJ index analysis, namely, the more unstable coupled system in f3-L and the dominant roles of the TH and ZA terms are robust across both MLD strategies.

According to the definition of the BJ index (see Eq. 3), each ocean dynamic term consists of two components: one related to the mean state and the other to air–sea feedback processes. Considering that both components may contribute to the differences in the TH and ZA terms between f3-L and f3-H, we calculate the relative contributions of each component to the total difference using a total derivative decomposition. As shown in Fig. 5a, the stronger TH term in f3-L compared to f3-H (bar 1) primarily arises from the difference in β_h (bar 4). The differences in μ_a and a_h make minor contributions, while the mean state differences and the covariance term make negative contributions. Thus, the dominant factor responsible for the stronger TH term in f3-L is the difference in β_h. Similarly, for the stronger ZA term in f3-L, the results (Fig. 5b) show that the difference in ZA term (bar 1) is primarily determined by the difference in β_u (bar 4), while the difference in a_h and the covariance term have marginal contributions.

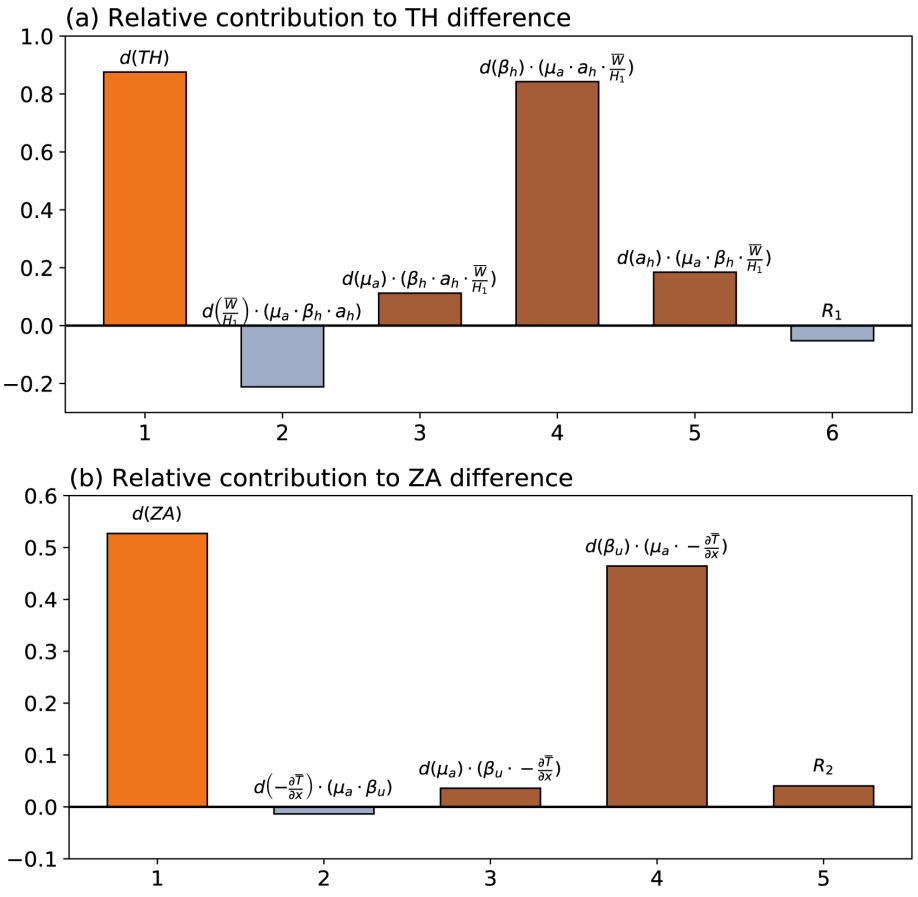

Figure 5. (a) Contributions of different components to the change in TH term. Bar 1 indicates the change in TH term [f3-L minus f3-H, d(TH)]. Bar 2 denotes the contribution from the mean state part change [$d(\overline{w}/H_1)$] to the change in TH term. Bar 3, 4 and 5 indicate the contributions from the air–sea feedbacks [$d(\mu_a)$, $d(\beta_h)$ and $d(a_h)$] to the change in TH term, respectively. Bar 6 is the residual, which denotes the contribution from the covariant changes of both the mean state part and the air–sea feedbacks. **(b)** Same as **(a)** but for the zonal advection feedback (ZA). Bar 1 indicate the change in ZA term [f3-L minus f3-H, d(ZA)]. Bar 2 denotes the contribution from the mean state part change [$d(\partial\overline{T}/\partial x)$] to the change in ZA term. Bar 3 and Bar 4 indicate the contributions from the air–sea feedbacks [$d(\mu_a)$ and $d(\beta_u)$], respectively. Bar 5 is the residual, representing the contribution from the covariant changes of both the mean state part and the air–sea feedbacks.

4.2 Resolution dependence of the β_h feedback process difference

The air–sea feedback process β_h represents the response of the equatorial Pacific thermocline tilt to τ_x'. Figure 6 shows the regression of thermocline depth anomalies onto zonal wind stress anomalies for the two models. Both models reproduce the expected pattern: in response to positive τ_x' over the equatorial Pacific, the anomalous thermocline depth (D') deepens in the eastern equatorial Pacific and shoals in the western equatorial Pacific. However, the response is much stronger in f3-L than in f3-H.

Based on the Sverdrup balance relationship (Jin, 1997; Li, 1997), the response of the D' to τ_x' is primarily determined by the mean equatorial thermocline depth ($\overline{H}$) and τ_x':

$$\frac{\partial D'}{\partial x} = \frac{\tau_x'}{\rho g \overline{H}}, \tag{17}$$

where ρ is the seawater density and g is the reduced gravity. We first examine the mean thermocline depth in both models and find that the difference in $\overline{H}$ between f3-L and f3-H is negligible (figure not shown). Therefore, the difference in $\overline{H}$ is not the primary cause.

Previous studies (Chen et al., 2015b; Chen et al., 2019a) have pointed out that the meridional structure of τ_x' is another key factor influencing the strength of β_h. Figure 7a presents the meridional structure of τ_x' for the two models and their difference (orange, f3-L minus f3-H). A significant difference exists: although the regression results show the same magnitude of τ_x' within the equatorial Pacific (5° S–5° N), the τ_x' in f3-L is meridionally more concentrated near the equator (0°) than that in f3-H. Since the τ_x' closer to equator is more effective in influencing D' (Chen et al., 2015b, 2019a), this more equatorially-confined meridional structure of τ_x' in

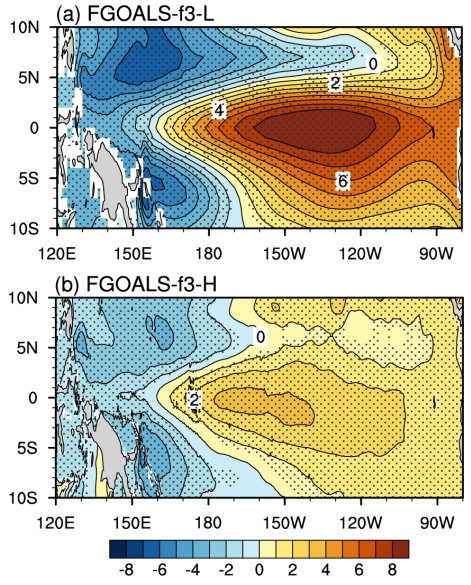

Figure 6. Distribution of the response of thermocline depth anomaly to zonal wind stress anomaly [β_h; units: m (N m^{-2})$^{-1}$] for **(a)** f3-L and **(b)** f3-H. Based on the linear relationship between sea surface height anomaly (SSHA) and thermocline depth anomaly (D'), the SSHA is used as a proxy of D'. The D' response to zonal wind stress anomaly is derived through regressing the SSHA field onto the averaged zonal wind stress anomaly over equatorial Pacific (5° S–5° N, 120° E–100° W). The stippling in this plot denotes the regression coefficient exceeding a confidence level of 99 % by using Student's t test.

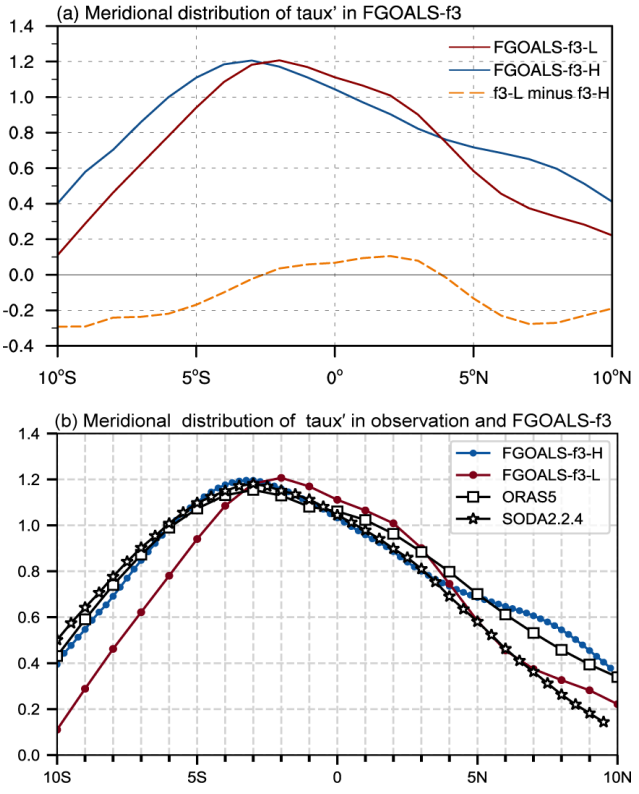

Figure 7. Meridional structure of normalized zonal wind stress anomalies [units: N m^{-2} (N m^{-2})$^{-1}$] averaged over the Niño4 longitude range (160° E–150° W) for **(a)** the result of f3-L (red solid line), f3-H (blue solid line) and their difference (orange dash line, f3-L minus f3-H). In this plot, all the data are both interpolated onto a 1° × 1° grid to facilitate the comparison; **(b)** the results of ORAS5 (black line marked by square, with a 1° × 1° grid), SODA2,2,4 (black line marked by asterisk, with a 0.25° × 0.25° grid), f3-L (red line marked by circle, with a 1° × 1° grid) and f3-H (blue line marked by circle, with a 0.25° × 0.25° grid). The normalized zonal wind stress anomalies are obtained by regressing the zonal wind stress anomalies field onto the Niño4 region (5° S–5° N, 160° E–150° W) averaged zonal wind stress anomalies.

f3-L inevitably results in a stronger response of D' to τ_x' (i.e., a larger β_h).

Furthermore, we compare the meridional structure of ENSO-related τ_x' in the two model versions with two reanalysis datasets. As shown in Fig. 7b, the meridional structures of τ_x' in the two reanalysis products (black lines) are very similar between 10° S–5° N, while some discrepancies exist within 5–10° N region. For the models, the f3-H (25 km atmospheric resolution) shows a τ_x' meridional structure in the equatorial region (5° S–5° N) that substantially resembles both reanalysis datasets. In contrast, the meridional structure of τ_x' within 5° S–5° N in f3-L (100 km atmospheric resolution) shows obvious discrepancies from the two reanalysis datasets. This suggests that model horizontal resolution can influence ENSO simulation by affecting the meridional distribution of τ_x'. The higher horizontal resolution is conducive to the more realistic representation of equatorial τ_x' meridional structure, thereby yielding a more reasonable thermocline feedback and ENSO amplitude.

4.3 Resolution dependence of the β_u feedback process

The air–sea feedback process β_u represents the response of the equatorial Pacific upper ocean zonal current anomaly (u_o') to τ_x'. Figure 8 shows the equatorial profile for the response of u_o' to τ_x' in both models. Both models simulate eastward u_o' in response to a unit eastward τ_x' in equatorial Pacific, but the response is significantly stronger in f3-L than in f3-H.

Considering that ENSO-related u_o' in the equatorial region is composed of anomalous zonal geostrophic currents (u_g') and anomalous Ekman currents (u_e') (see Sect. 2.3.4), we first diagnose the response of u_g' and u_e' to wind stress anomalies (Fig. 9). In both versions, the response of u_o' to τ_x' is primarily contributed by the response of u_g' to τ_x', while the contribution of u_e' is much smaller. This indicates that the difference in u_g' response to τ_x' is the main cause of the difference in β_u between the two model versions. Based on the geostrophic formula (Eq. 12), the magnitude of u_g' is related to the second-order meridional derivative of D'. Since the meridional structure of D' (Fig. 6) exhibits a

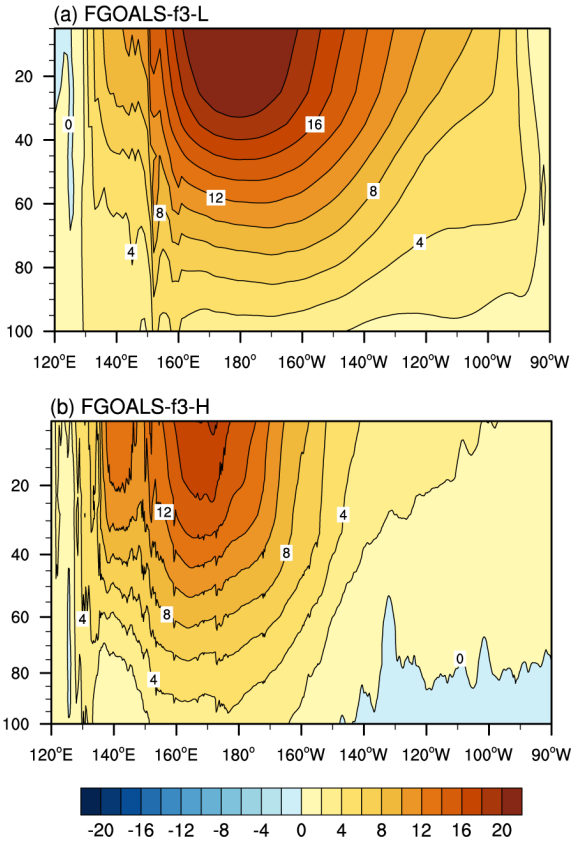

Figure 8. Vertical profile (averaged over 5° S–5° N) of the response of zonal ocean current anomaly (u'_o) to the zonal wind stress anomaly [β_u; units: m s^{-1} (N m^{-2})$^{-1}$] for **(a)** f3-L and **(b)** f3-H. The u'_o response to zonal wind stress anomaly is derived through regressing the u'_o field onto the averaged zonal wind stress anomaly over equatorial Pacific (5° S–5° N, 120° E–100° W).

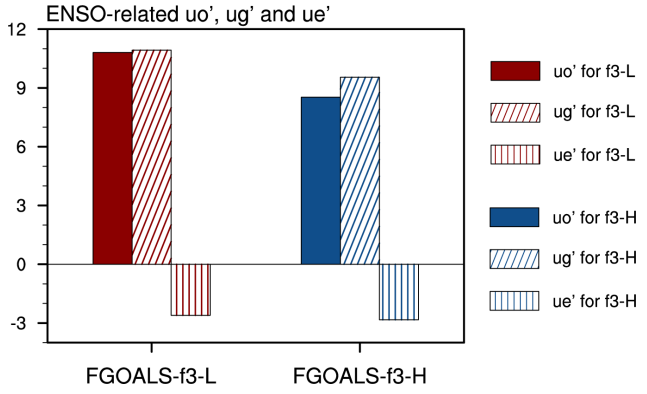

Figure 9. The ENSO-related zonal current anomalies (u') averaged over 0–65 m, zonal geostrophic current anomalies (u'_g) and zonal Ekman current anomalies (u'_e) along the equatorial eastern Pacific (2° S–2° N, 180–80° W) for f3-L (red bar) and f3-H (blue bar). The ENSO-related zonal current anomalies, zonal geostrophic current anomalies and zonal Ekman current anomalies are obtained by regressing it anomalies field onto the zonal wind stress anomalies averaged over Niño4 region (5° S–5° N, 160° E–150° W), respectively.

parabolic shape (peaking at equator and decreasing poleward), a stronger D' in the equatorial region corresponds to a larger value of second-order meridional derivative $\left(-\frac{\partial^2 D'}{\partial y^2}\right)$ and, consequently, a stronger u'_g. As the D' response to τ'_x is primarily modulated by the β_h process, the difference in the β_u between the f3-L and f3-H is also primarily attributed to difference in the β_h process. That is, the stronger β_h in f3-L leads to a stronger D', which in turn induces a stronger u'_g and u'_o and ultimately results in a stronger β_u.

4.4 Comparison with OMIP simulations

It should be noted that although our conclusions drawn from Coupled General Circulation Model (CGCM) indicate that the improved ENSO simulation is closely linked to the increased atmospheric resolution, the potential influence of oceanic horizontal resolution on ENSO simulation also merits its brief examination. For instance, from the perspective of the oceanic component of CGCM (OGCM), Li et al. (2025) examined the oceanic zonal current and thermocline depth anomalies to zonal wind forcing by analyzing the outputs from Ocean Model Intercomparison Project 2 (OMIP2, Griffies et al., 2016) and found that the oceanic response to wind forcing is a key factor influencing ENSO simulation. Therefore, the resolution-induced contrast between the OMIP experiment and the CMIP experiment (i.e., the "historical" experiment) is a noteworthy phenomenon that warrants explanation.

According to the CMIP6's protocol, OMIP2 experiments are forced by the identical atmospheric reanalysis datasets, thus providing an ideal framework to isolate biases originating from the oceanic component. Both f3-L and f3-H have participated in OMIP2, with respective oceanic horizontal resolutions of approximately 1 and 0.1°. To further assess the potential impact of oceanic horizontal resolution on ENSO simulation, we compare the key air–sea feedback terms (β_h and β_u) between f3-L and f3-H OMIP2 outputs. As shown in Fig. 10, the response of zonal current and thermocline depth anomalies to the identical τ'_x are remarkably similar between the two ocean models. This indicates that the differences in OGCM resolution itself may not be the primary driver of the differences in β_h and β_u. Moreover, this finding (Fig. 10) stands in stark contrast to the large differences in β_h and β_u identified in the two coupled simulations (Figs. 6 and 8).

To understand the contrasting OMIP–CMIP behavior, we compare the meridional structures of the "normalized τ'_x" between the CMIP and OMIP experiments for both model versions, as shown in Fig. S5. Here the normalized τ'_x is obtained by regressing the τ'_x field onto Niño4-region-averaged τ'_x; and then averaging over the Niño4 longitude range (160° E–150° W). This normalization procedure enables a fair com-

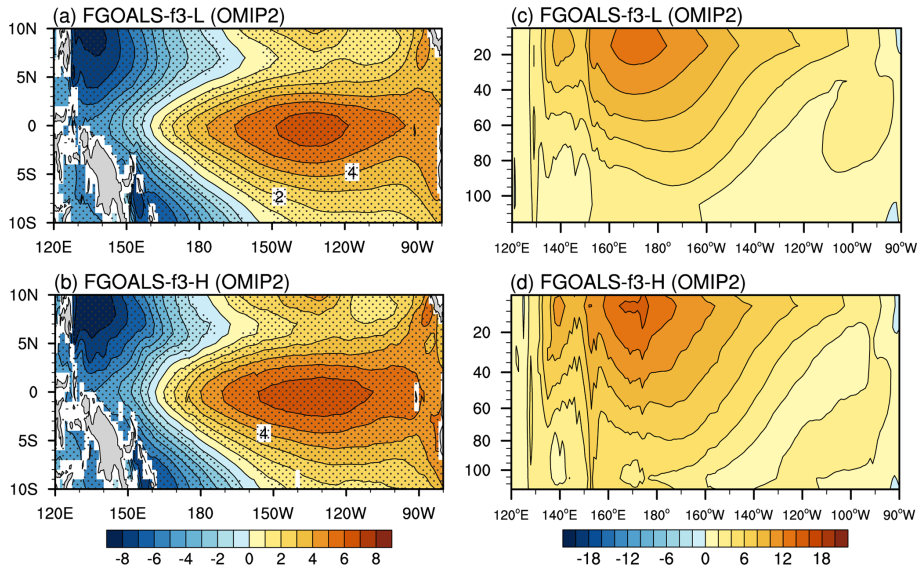

Figure 10. **(a)–(d)** are same as Figs. 6 and 8, respectively, but for the OMIP2 simulations.

Table 3. Meridional distribution index (MDI; units: °) of τ_x', calculated from the meridional structure of normalized τ_x' as shown in Fig. B6.

	f3-L	f3-H
CMIP	2.55	2.71
OMIP	2.68	2.64

parison of the meridional structure of τ_x' across different experiments and model versions. In f3-L, the CMIP experiment produces stronger τ_x' near the equator compared to the OMIP forcing that was derived from the JRA55-do reanalysis (red lines in Fig. S5). This leads to an enhanced thermocline response in CMIP relative to OMIP. Conversely, in f3-H, the CMIP experiment yields weaker equatorial τ_x' than the OMIP forcing (blue lines in Fig. S5), resulting in a weaker thermocline response in CMIP relative to OMIP.

Furthermore, we quantify these structural differences in τ_x' between the CMIP and OMIP experiments based on the MDI metric, as introduced in Sect. 2.3.3. The qualitative differences in τ_x' distributions shown in Fig. S5 are corroborated by the MDI results (Table 3). In f3-L, the CMIP experiment yields a notably smaller MDI (2.55°) than the OMIP experiment (2.68°), indicating a more equatorially concentrated τ_x' structure that can more efficiently drive thermocline variability, and hence produces a larger β_h in the CMIP experiment. Conversely, in f3-H, the CMIP experiment exhibits a larger MDI (2.71°) than the OMIP experiment (2.64°), corresponding to a broader τ_x' distribution that drives a more moderate thermocline response and a smaller β_h.

Therefore, the evidence from the OMIP2 experiments corroborates our main conclusion: the refined atmospheric horizonal resolution, which more realistically captures the meridional structure of τ_x', plays a decisive role in improving the simulation of the key air–sea feedbacks (β_h and β_u) and ENSO amplitude in FGOALS-f3 model. Nevertheless, a more comprehensive investigation, potentially involving finer oceanic resolutions and their interactions with the atmosphere, deserves further exploration in the future.

5 Diagnostic of oscillation regularity

5.1 Resolution dependence of ENSO irregularity: differences in HF wind activity

A large body of studies have suggested that the HF zonal wind activity over the western and central equatorial Pacific (WCEP) plays a crucial role in the onset and development of ENSO events (Rong et al., 2011; Chen et al., 2017). In general, this HF zonal wind activity refers to westerly wind event (WWE) and easterly wind event (EWE) with time scales less than 90 d. Due to their transient, intense, and somewhat random nature, the HF zonal wind forcing is also considered as an important factor contributing to the diversity and irregularity of ENSO (Chen et al., 2015a; Fedorov et al., 2015). Motivated by this, we hypothesize that the difference in the ENSO regularity between f3-L and f3-H may arise from the differences in HF zonal wind activity.

To test this, we calculate the intensity of the HF zonal wind activity based on the Eqs. (14) and (15). Figure 11 shows the WWI and EWI index that measures the cumulative sum of HF westerly (easterly) wind anomalies over WCEP during the ENSO development period, for the observation and

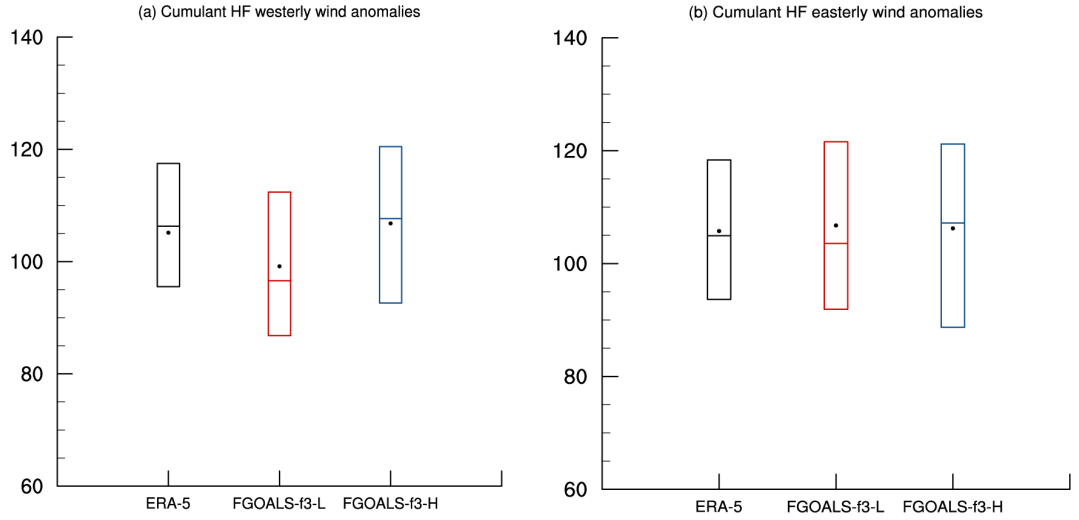

Figure 11. The boxplots of the **(a)** WWI index and **(b)** EWI index during the ENSO development phase (January to August). Red, blue and black boxes indicate the f3-L, f3-H and observations, respectively. The upper and lower boundaries of the box represent the 75th and 25th percentile values, respectively. The horizontal line in the box represents the median. The black dot represents the average value.

the two model versions. As shown in Fig. 11a, the intensity of HF westerlies in f3-H is comparable to that in the observation, with similar mean and median values. However, f3-L simulates much weaker intensity of HF westerlies. For HF easterly activity (Fig. 11b), both models show comparable statistics to the observation, with no significant differences between f3-L and f3-H. Overall, these results indicate that f3-L strongly underestimates HF westerly wind activity relative to the f3-H and the observation.

HF westerly wind activities are considered as semi-stochastic perturbations that modulate ENSO evolution (Gebbie et al., 2007; Gebbie and Tziperman, 2009). On the one hand, their occurrence is partly influenced by ENSO-related SSTA (Sun et al., 2020), but is also regarded as random noise independent of ENSO system (Moore and Kleeman, 1999). Most ENSO theoretical models treat HF westerly wind activity as external white noise forcing (Eisenman et al., 2005). This implies that the impact of HF activity on the coupled system depends, to some extent, on its relative magnitude relative to the ENSO amplitude. Notably, the aforementioned analysis based on the BJ index (a linear framework that excludes nonlinear processes like atmospheric "noise") has shown that the coupled system simulated by f3-L is more unstable than that of f3-H, hence the ENSO variability in f3-L is more prone to self-sustained oscillation. Considering that the HF wind activities in f3-L is also significantly weaker than that in f3-H, from the perspective of signal-to-noise ratio, this weaker "noise" is insufficient to "disrupt" the overly strong ENSO oscillation in f3-L, allowing its ENSO cycle to evolve in a regular and self-sustained manner.

To further quantify the relative magnitude of stochastic atmospheric forcing compared to the ENSO signal, we introduce an NSR metric, as introduced in Sect. 2.3.5. A larger NSR indicates stronger stochastic forcing relative to the ENSO signal. The NSR values are 2.67, 1.98, and 4.73 ($m\,s^{-1}\,K^{-1}$) for the observation, f3-L, and f3-H, respectively. The substantially smaller NSR in f3-L reflects the combination of its weaker HF wind activity and stronger ENSO amplitude, confirming that the stochastic forcing in f3-L is insufficient to disrupt its overly intense ENSO oscillation. In contrast, the larger NSR in f3-H indicates that stronger stochastic forcing acts on a weaker ENSO signal, facilitating the irregular oscillation that more closely resembles the observation.

5.2 Sources of differences in HF westerly wind activity: evaluation of TC and MJO

To further explore the origin of difference in HF westerly wind intensity between f3-L and f3-H, we compare the simulated performance of TC and MJO activities in these two models. The results show that the differences in the HF westerly wind intensity are primarily related to the models' ability to reproduce TC activity. Figure 12 shows the spatial distribution of TCTD over the western North Pacific (WNP). The spatial distributions of TCTD in both f3-H and f3-L are similar to the observation, with TC tracks primarily located in the southwestern quadrant of WNP. Although both versions can reasonably reproduce the spatial distribution characteristics of TC activities over the WNP, a significant difference exists in TC frequency: TC activity is much more frequent in f3-H than that in f3-L. The difference map (Fig. 12d, f3-H minus f3-L) shows positive values almost everywhere north of the equator. It is worth noting that TCTD in f3-H remains relatively weak compared to the observation, which is a common

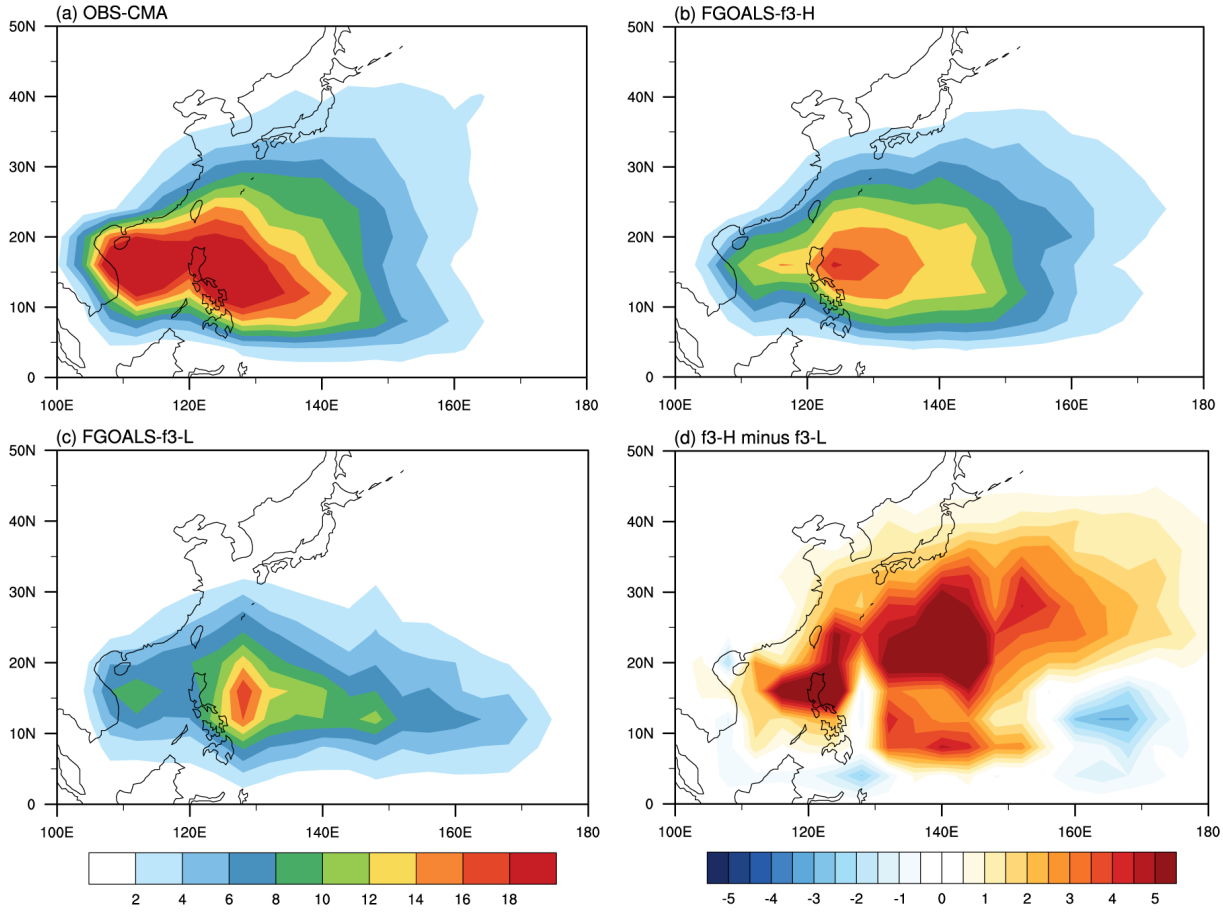

Figure 12. The averaged TC track density (TCTD, units: counts per year) over western North Pacific for **(a)** observation (CMA), **(b)** f3-H, **(c)** f3-L and **(d)** the difference between f3-H and f3-L (f3-H minus f3-L).

simulation bias in most current climate models (Nakamura et al., 2017; Tang et al., 2022). Although f3-H still underestimates TC activity compared to the observation, this improvement relative to f3-L is substantial.

Furthermore, we compare the difference in the TC intensity between f3-H and f3-L. Figure 13 shows the spatial distribution of ACE index over WNP in the observation and the models. Both models show that strong TC activity is primarily concentrated east of the Philippines sea, consistent with the observation (Ma et al., 2025). However, the ACE index in f3-H is significantly stronger than that in f3-L, indicating stronger TC activity in f3-H. In summary, the TC activity over WNP is more frequent and intense in f3-H than that in f3-L, which largely explains the stronger HF westerly wind anomalies in f3-H.

Model horizontal resolution is a key factor in TC simulation (Tang et al., 2022). In general, climate models with coarse resolutions ($\geq$ 100 km) tend to only reproduce TC-like structures (Camargo et al., 2005; Camargo and Wing, 2016), with activity that is relatively weak and infrequent (Camargo, 2013; Nakamura et al., 2017). As resolution increases, models can simulate more frequent and more intense TC activity (Roberts et al., 2020a; Tang et al., 2022). In particular, when the horizontal resolution is increased to 25 km, the simulation of TC spatial structure and associated wind fields is significantly improved, yielding more realistic characteristics of TC activity (Davis, 2018; Roberts et al., 2020b). The analysis results of the FGOALS-f3 models (Figs. 11 and 12) are consistent with these previous findings. Compared to the f3-L model (with a horizontal resolution of 100 km), the f3-H model (with a horizontal resolution of 25 km) provides a more realistic simulation of TC frequency and produces stronger TC intensities. This difference in TC simulation associated with model resolution modulates the intensity of HF westerly wind activity and hence influences the regularity of ENSO cycle in the two models.

On the other hand, we also examine the other primary source of HF westerly wind activity – the MJO. Figure 14 shows the wavenumber-frequency spectra of the space-time filtered precipitation and surface zonal wind. It can be seen that the spectral peak of precipitation and surface zonal wind in both models are concentrated at 30–80 d period, consistent with the observation. This indicates that both models reproduce the observed MJO timescales reasonably well. In

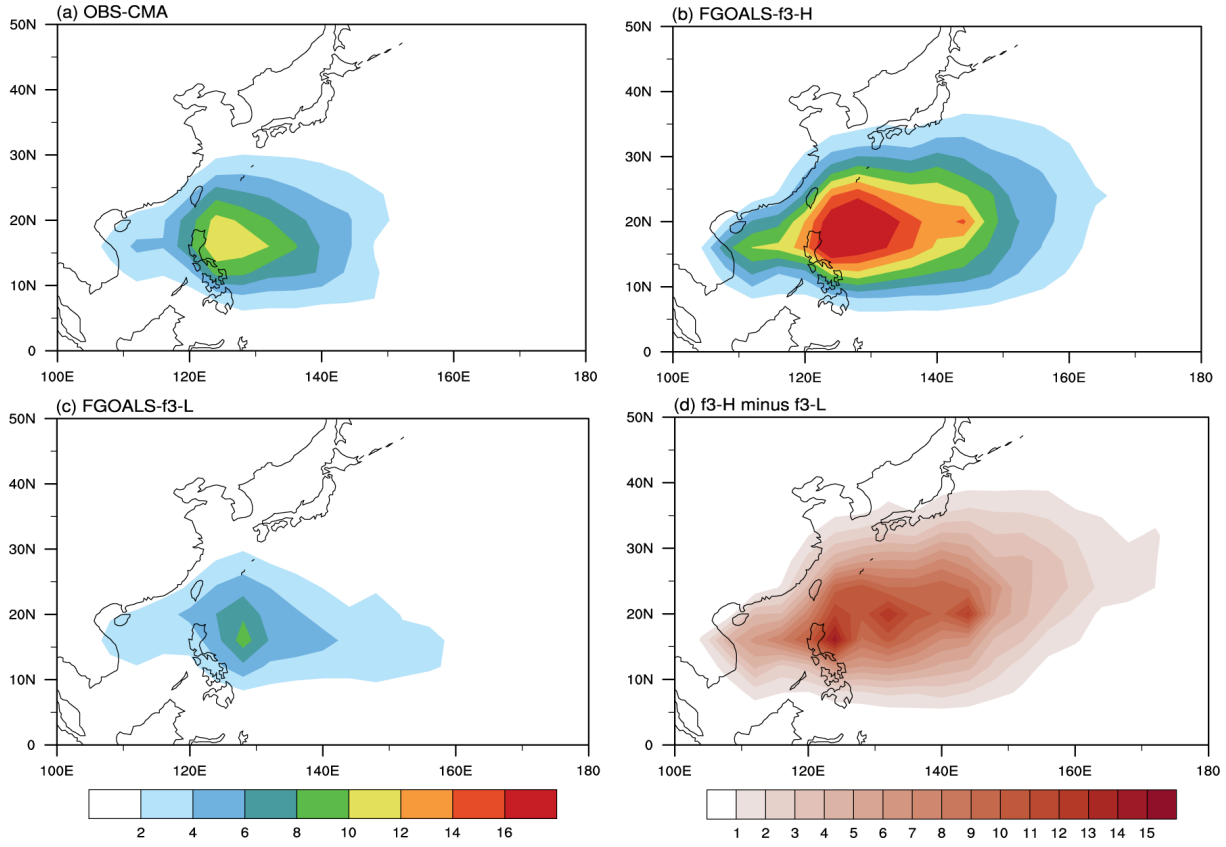

Figure 13. The averaged accumulated cyclone energy (ACE, units: 10^4 kn yr^{-1}) over western North Pacific for **(a)** observation (CMA), **(b)** f3-H, **(c)** f3-L and **(d)** the difference between f3-H and f3-L (f3-H minus f3-L).

terms of intensity, although the MJO-related precipitation and zonal wind fields are somewhat exaggerated in both models compared to the observation, the difference between f3-L and f3-H is small, especially for MJO-related zonal winds. Therefore, the difference in HF westerly wind activity is likely not directly linked to MJO activity.

Although finer resolution may improve model performance in certain aspects, these preliminary results show no significant improvement in MJO simulation from 100 to 25 km in the case of these two FGOALS-f3 models. On the one hand, this may be because MJO simulation is heavily constrained by the accurate representation of physical processes like convection parameterization, boundary layer processes, and air–sea coupling. Thus, increased resolution must be combined with optimized physics schemes to effectively improve MJO simulation (Jiang et al., 2020b). On the other hand, recent studies suggest that significant MJO improvement can be seen when resolution increases to the kilometer-scale – the "convection-permitting resolution" (Savarin and Chen, 2022).

In summary, we find that the high-resolution version can better simulate TC activity, with more frequent and stronger TCs over the WNP than the lower-resolution version. This difference results in stronger HF westerly wind activity in f3-H than that in f3-L. Given that HF westerly wind activity acts as a stochastic forcing on ENSO, the relatively weaker HF atmospheric noise in f3-L has a limited randomizing effect on its stronger ENSO signal. In other words, the weaker HF zonal wind activity in f3-L cannot overcome its inherently stronger ENSO signal, leading to overly regular oscillation in f3-L. In contrast, f3-H has a weaker intrinsic ENSO signal but stronger "noise"" Therefore, the ENSO cycle in f3-L appears much more regular than that in f3-H.

6 Conclusions and implications

6.1 Conclusions

This study provides a process-based evaluation of how horizontal resolution influences ENSO simulation in the CAS FGOALS-f3 climate system model. The comparison between its low-resolution (f3-L, $\sim$ 100 km) and high-resolution (f3-H, $\sim$ 25 km) configurations reveals systematic and resolution-dependent differences in ENSO amplitude, period, oscillation irregularity, and underlying air–sea coupling processes.

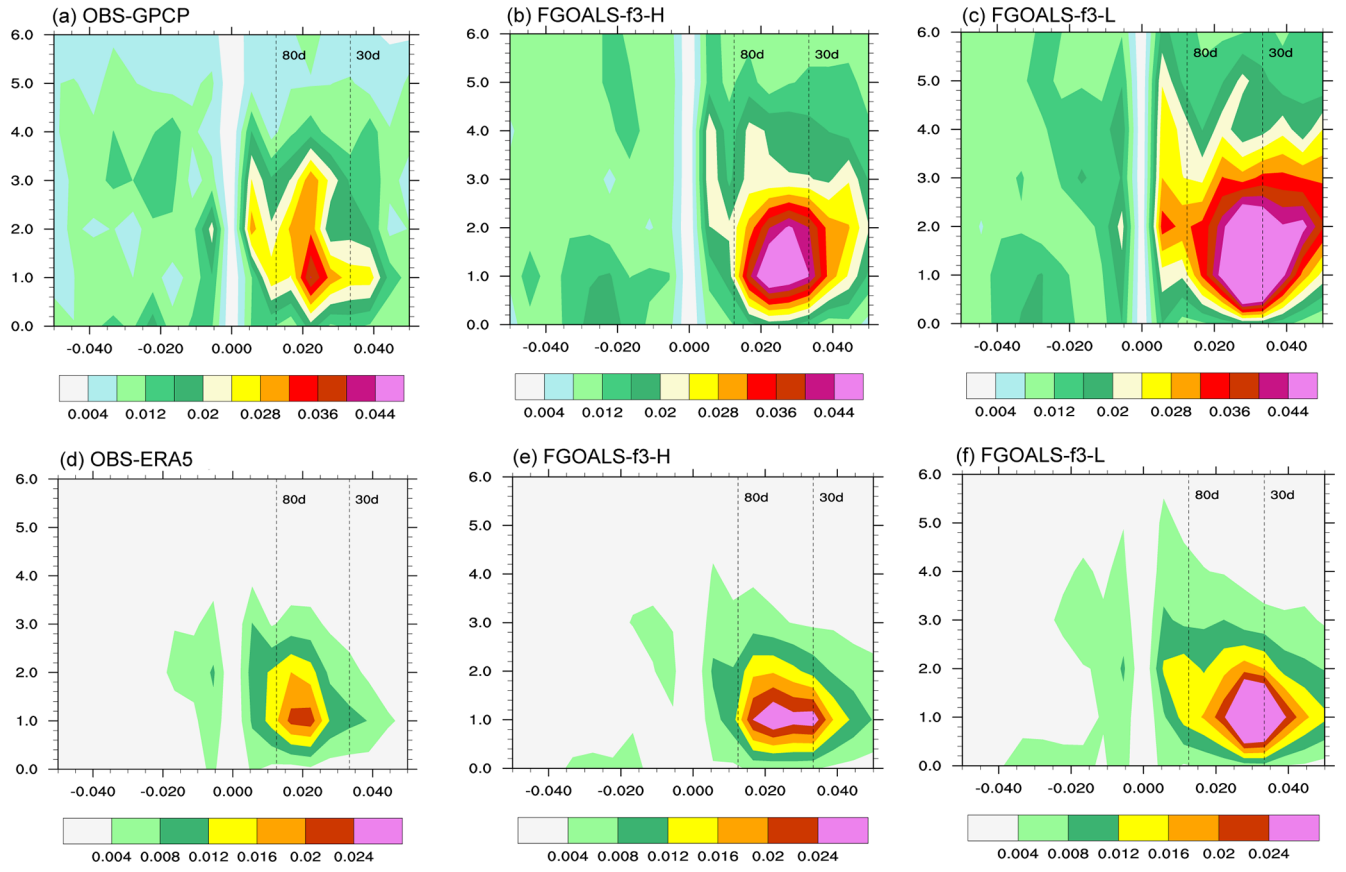

Figure 14. Wavenumber-frequency spectra of space-time filtered **(a–c)** precipitation (units: mm d^{-1}) and **(d–f)** surface zonal wind fields (m s^{-1}) during the boreal winter (November to next August) for observation **(a, d)**, f3-H **(b, e)** and f3-L **(c, f)**.

A key structural source of bias in f3-L is the overly confined meridional structure of ENSO-related zonal wind stress anomalies, which strengthens the thermocline and zonal-advection feedbacks and leads to an exaggerated ENSO amplitude. The process-oriented diagnosis based on ENSO-related air–sea coupling processes demonstrates that these feedbacks can be directly attributed to resolution-sensitive meridional distribution of equatorial zonal wind stress anomalies, indicating that resolving the meridional structure of wind forcing is essential for realistic representation of ENSO amplitude.

The excessive regularity of ENSO in f3-L is another resolution-driven bias, arising from insufficient HF atmospheric variability. The high-resolution configuration produces more realistic TC activity and more vigorous WWEs, which introduce stochastic forcing that disrupts the ENSO cycle and generates irregular variability closer to the observation. These results highlight that the representation of synoptic-scale atmospheric processes is integral to capturing observed temporal irregularity of ENSO.

Overall, this study demonstrates that ENSO-related biases in FGOALS-f3 arise from identifiable, resolution-sensitive structural features in the coupled system. Through two complementary diagnostic pathways, we provide a traceable and mechanistic explanation for how horizontal resolution modulates ENSO simulation (Fig. 15). The diagnostic framework developed here is model-agnostic and reproducible, offering a practical tool for evaluating ENSO performance in other climate models and guiding future development of the FGOALS model family.

6.2 Implications

The findings from this study yield several actionable insights for FGOALS-f3 development and for the broader CMIP-class modeling community. (1) Improving the atmospheric representation of equatorial wind stress meridional gradient should be a development priority. (2) As shown in Fig. 15, increase in horizontal resolution has impacts on ENSO dynamics from both deterministic and stochastic pathways: the deterministic aspect influencing ENSO behaviors is via air–sea coupling processes, and the stochastic aspect influencing ENSO behaviors is via HF wind activity, both of which should be explicitly considered in future model evaluation framework. (3) The diagnostics applied here are model-agnostic and can serve as a reproducible framework for as-

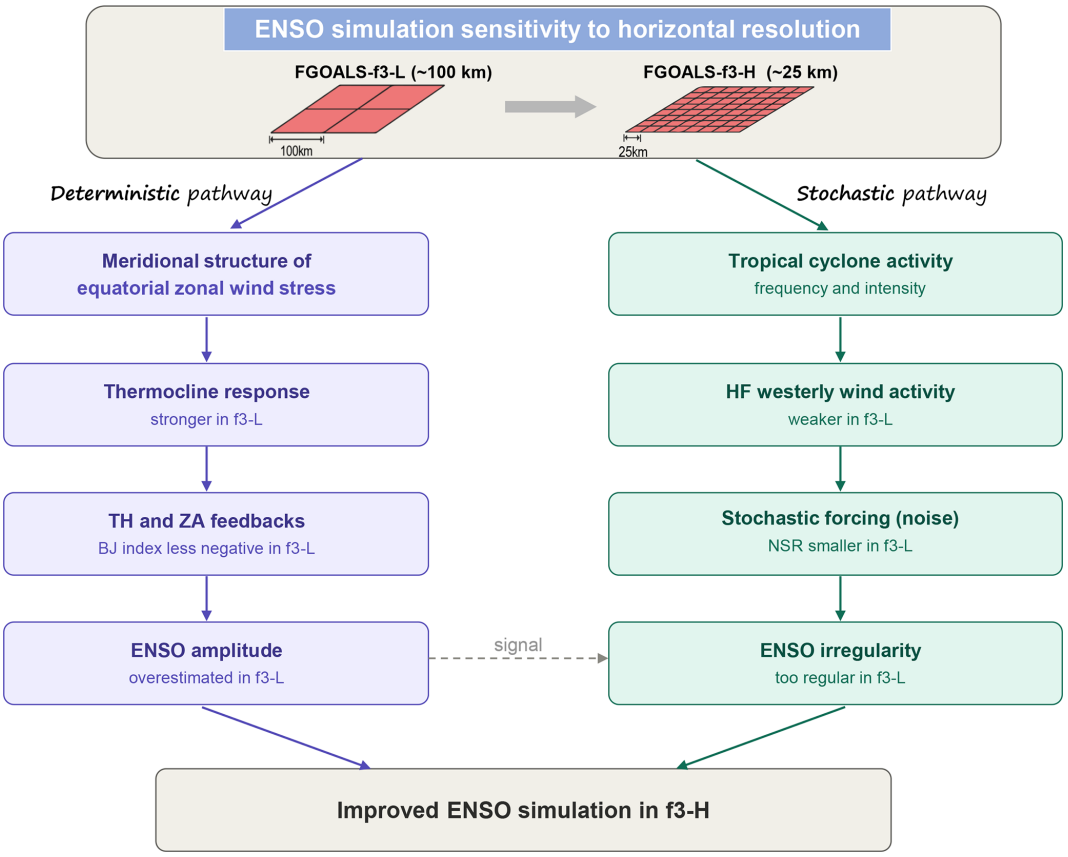

Figure 15. Schematic diagram illustrating how increased horizontal resolution (∼ 100 to ∼ 25 km) improves ENSO simulation in FGOALS-f3 via both the deterministic feedback processes and the stochastic atmospheric forcing pathways.

sessing resolution effects in other climate models participating in CMIP6/CMIP7. We encourage the community to adopt the process-oriented diagnostics presented here as a complement to conventional statistical metrics, so that the improvements in ENSO simulation can be traced back to specific physical mechanisms rather than assessed solely by outcome-based indices. (4) The ∼ 25 km atmosphere resolution of f3-H improves both the air–sea coupling processes and the stochastic forcing mechanisms, supporting the ongoing efforts toward next-generation high-resolution climate models. However, the computational cost increases substantially from f3-L to f3-H. The low-resolution version runs on 384 processor cores and achieves a throughput of approximately 15–20 model years per wall-clock day, whereas the high-resolution version requires 6,144 processor cores and achieves only ∼ 0.25 model years per wall-clock day. This sharp increase in computational expense makes century-scale ensemble simulations with high-resolution models, such as f3-H, considerably more demanding. Such a cost–benefit trade-off further motivates the development of variable-resolution modeling frameworks (e.g., the Model for Prediction Across Scales and the ICOsahedral Nonhydrostatic model), which can selectively refine the grid over the tropical Pacific to capture these resolution-sensitive processes while maintaining coarser resolution elsewhere.

Code and data availability. Source codes of the FGOALS-f3 model used in this study and the analysis scripts are archived at https://doi.org/10.5281/zenodo.19552337 (Song et al., 2026). The model output of FGOALS-f3 models described in this paper is distributed through the Earth System Grid Federation (ESGF) and is freely obtained via the ESFG data portals after registration (https://aims2.llnl.gov/search, last access: 28 May 2026). All the observation and reanalysis datasets are available online and publicly available as cited in the references. The ORAS5 and ERA-5 datasets are obtained from https://cds.climate.copernicus.eu/datasets (last access: 28 May 2026). The HadISST dataset is from https://www.metoffice.gov.uk/hadobs/hadisst/data/download.html (last access: 28 May 2026). The GPCP dataset is available at https://www.ncei.noaa.gov/data/global-precipitation-climatology-project-gpcp-daily/access (last access: 28 May 2026). The SODA2.2.4 dataset can be accessed at http://apdrc.soest.hawaii.edu/datadoc/soda_2.2.4.php (last access: 28 May 2026). The CMA TC best track dataset is from https://tcdata.typhoon.org.cn/en/zjljsjj.html (last access: 28 May 2026). The description and data for HighResSST-present simulations of FGOALS-f3 can be found at

https://doi.org/10.22033/ESGF/CMIP6.3312 (Bao and He, 2019; Bao et al., 2020).

Supplement. The supplement related to this article is available online at https://doi.org/10.5194/gmd-19-4725-2026-supplement.

Author contributions. All authors contributed to the study conception and design. Material preparation, data collection and analysis were performed by MS and LC. JZ contributed to the application of methods related to TC detection. The first draft of the manuscript was written by MS and LC. QY, BA and HZ discussed the results and commented on the manuscript. All authors read and approved the final manuscript.

Competing interests. The contact author has declared that none of the authors has any competing interests.

Disclaimer. Publisher's note: Copernicus Publications remains neutral with regard to jurisdictional claims made in the text, published maps, institutional affiliations, or any other geographical representation in this paper. The authors bear the ultimate responsibility for providing appropriate place names. Views expressed in the text are those of the authors and do not necessarily reflect the views of the publisher.

Acknowledgements. We acknowledge the High Performance Computing Center of Nanjing University of Information Science & Technology for their support of this work.

Financial support. This work was jointly supported by the National Key Research and Development Program of China (grant no. 2022YFF0802000), NSFC (grant no. 42576024), the Excellent Youth Natural Science Foundation of Jiangsu Province (grant no. BK20230061) and Postgraduate Research & Practice Innovation Program of Jiangsu Province (grant no. KYCX24_1417).

Review statement. This paper was edited by Xianan Jiang and reviewed by Shizuo Liu and one anonymous referee.

References

Adler, R. F., Huffman, G. J., Chang, A., Ferrao, R., Xie, P.-P., Janowiak, J., Rudolf, B., Schneiser, U., Curtis, S., Bolvin, D., Gruber, A., Susskind, J., Arkin, P., and Nelkin, E.: The version-2 global precipitation climatology project (GPCP) monthly precipitation analysis (1979–present), J. Hydrometeorol., 4, 1147–1167, https://doi.org/10.1175/1525-7541(2003)004<1147:TVGPCP>2.0.CO;2, 2003.

An, B., Yu, Y. Q., Bao, Q., He, B., Li, J. X., Luan, Y. H., Chen, K. J., and Zheng, W. P.: CAS FGOALS-f3-H dataset for the high-resolution model intercomparison project (HighResMIP) Tier 2, Adv. Atmos. Sci., 39, 1873–1884, https://doi.org/10.1007/s00376-022-2030-5, 2022.

Bacmeister, J. T., Wehner, M. F., Neale, R. B., Gettelman, A., Hannay, C., Lauritzen, P. H., Caron, J. M., and Truesdale, J. E.: Exploratory high-resolution climate simulations using the community atmosphere model (CAM), J. Climate, 27, 3073–3099, https://doi.org/10.1175/jcli-d-13-00387.1, 2014.

Bao, Q. and He, B.: CAS FGOALS-f3-H model output prepared for CMIP6 HighResMIP highresSST-present, Earth System Grid Federation [data set], https://doi.org/10.22033/ESGF/CMIP6.3312, 2019.

Bao, Q., Liu, Y. M., Wu, G. X., He, B., Li, J. X., Wang, L., Wu, X. F., Chen, K. J., Wang, X. C., Yang, J., and Zhang, X. Q.: CAS FGOALS-f3-H and CAS FGOALS-f3-L outputs for the high-resolution model intercomparison project simulation of CMIP6, Atmos. Ocean. Sci. Lett., 13, 576–581, https://doi.org/10.1080/16742834.2020.1814675, 2020.

Barnston, A. G., Tippett, M. K., L'Heureux, M. L., Li, S., and DeWitt, D. G.: Skill of real-time seasonal ENSO model predictions during 2002–11: Is our capability increasing?, B. Am. Meteorol. Soc., 93, 631–651, https://doi.org/10.1175/bams-d-11-00111.1, 2012.

Bell, G. D., Halpert, M. S., Schnell, R. C., Higgins, R. W., Lawrimore, J., Kousky, V. E., Tinker, R., Thiaw, W., Chelliah, M., and Artusa, A.: Climate assessment for 1999, B. Am. Meteorol. Soc., 81, s1–s50, https://doi.org/10.1175/1520-0477(2000)81[s1:CAF]2.0.CO;2, 2000.

Cai, W. J., Santoso, A., Collins, M., Dewitte, B., Karamperidou, C., Kug, J.-S., Lengaigne, M., McPhaden, M. J., Stuecker, M. F., Taschetto, A. S., Timmermann, A., Wu, L. X., Yeh, S.-W., Wang, G., Ng, B., Jia, F., Yang, Y., Ying, J., Zheng, X.-T., Bayr, T., Brown, J. R., Capotondi, A., Cobb, K. M., Gan, B., Geng, T., Ham, Y.-G., Jin, F.-F., Jo, H.-S., Li, X., Lin, X., McGregor, S., Park, J.-H., Stein, K., Yang, K., Zhang, L., and Zhong, W. X.: Changing El Niño–Southern Oscillation in a warming climate, Nat. Rev. Earth Environ., 2, 628–644, https://doi.org/10.1038/s43017-021-00199-z, 2021.

Camargo, S. J.: Global and regional aspects of tropical cyclone activity in the CMIP5 models, J. Climate, 26, 9880–9902, https://doi.org/10.1175/jcli-d-12-00549.1, 2013.

Camargo, S. J. and Wing, A. A.: Tropical cyclones in climate models, Wires Clim. Change, 7, 211–237, https://doi.org/10.1002/wcc.373, 2016.

Camargo, S. J., Barnston, A. G., and Zebiak, S. E.: A statistical assessment of tropical cyclone activity in atmospheric general circulation models, Tellus A, 57, 589–604, https://doi.org/10.3402/tellusa.v57i4.14705, 2005.

Carton, J. A. and Giese, B. S.: A Reanalysis of Ocean Climate Using Simple Ocean Data Assimilation (SODA), Mon. Weather Rev., 136, 2999–3017, https://doi.org/10.1175/2007mwr1978.1, 2008.

Chang, P., Zhang, S. Q., Danabasoglu, G., Yeager, S. G., Fu, H. H., Wang, H., Castruccio, F. S., Chen, Y., Edwards, J., Fu, D., Jia, Y., Laurindo, L. C., Liu, X., Rosenbloom, N., Small, R. J., Xu, G. P., Zeng, Y. H., Zhang, Q. Y., Bacmeister, J., Bailey, D. A., Duan, X., DuVivier, A. K., Li, D. P., Li, Y. X., Neale, R., Stössel, A., Wang, L., Zhuang, Y., Baker, A., Bates, S., Dennis, J., Diao, X., Gan, B. L., Gopal, A., Jia, D. N., Jing, Z., Ma, X., Saravanan, R., Strand, W. G., Tao, J., Yang, H. Y., Wang, X. Q., Wei, Z. Q., and Wu, L. X.: An unprecedented set of high-resolution earth system simulations for understanding multiscale interactions in climate variability and change, J. Adv. Model. Earth Syst., 12, e2020MS002298, https://doi.org/10.1029/2020ms002298, 2020.

Chen, D. K., Lian, T., Fu, C., Cane, M. A., Tang, Y. M., Murtugudde, R., Song, X. S., Wu, Q. Y., and Zhou, L.: Strong influence of westerly wind bursts on El Niño diversity, Nat. Geosci., 8, 339–345, https://doi.org/10.1038/ngeo2399, 2015a.

Chen, L., Li, T., and Yu, Y. Q.: Causes of strengthening and weakening of ENSO amplitude under global warming in four CMIP5 models, J. Climate, 28, 3250–3274, https://doi.org/10.1175/jcli-d-14-00439.1, 2015b.

Chen, L., Yu, Y. Q., and Zheng, W. P.: Improved ENSO simulation from climate system model FGOALS-g1.0 to FGOALS-g2, Clim. Dynam., 47, 2617–2634, https://doi.org/10.1007/s00382-016-2988-8, 2016a.

Chen, L., Li, T., Behera, S. K., and Doi, T.: Distinctive precursory air–sea signals between regular and super El Niños, Adv. Atmos. Sci., 33, 996–1004, https://doi.org/10.1007/s00376-016-5250-8, 2016b.

Chen, L., Li, T., Wang, B., and Wang, L.: Formation mechanism for 2015/16 super El Nino, Sci. Rep.-UK, 7, 2975–2985, https://doi.org/10.1038/s41598-017-02926-3, 2017.

Chen, L., Wang, L., Li, T., and Liu, J.: Drivers of reduced ENSO variability in mid-Holocene in a coupled model, Clim. Dynam., 52, 5999–6014, https://doi.org/10.1007/s00382-018-4496-5, 2019a.

Chen, L., Zheng, W., and Braconnot, P.: Towards understanding the suppressed ENSO activity during mid-Holocene in PMIP2 and PMIP3 simulations, Clim. Dynam., 53, 1095–1110, https://doi.org/10.1007/s00382-019-04637-z, 2019b.

Craig, A. P., Vertenstein, M., and Jacob, R.: A new flexible coupler for earth system modeling developed for CCSM4 and CESM1, Int. J. High Perform. C., 26, 31–42, https://doi.org/10.1177/1094342011428141, 2012.

Davis, C. A.: Resolving tropical cyclone intensity in models, Geophys. Res. Lett., 45, 2082–2087, https://doi.org/10.1002/2017GL076966, 2018.

Dawson, A., Matthews, A. J., Stevens, D. P., Roberts, M. J., and Vidale, P. L.: Importance of oceanic resolution and mean state on the extra-tropical response to El Niño in a matrix of coupled models, Clim. Dynam., 41, 1439–1452, https://doi.org/10.1007/s00382-012-1518-6, 2013.

Docquier, D., Grist, J. P., Roberts, M. J., Roberts, C. D., Semmler, T., Ponsoni, L., Massonnet, F., Sidorenko, D., Sein, D. V., Iovino, D., Bellucci, A., and Fichefet, T.: Impact of model resolution on Arctic sea ice and North Atlantic Ocean heat transport, Clim. Dynam., 53, 4989–5017, https://doi.org/10.1007/s00382-019-04840-y, 2019.

Eisenman, I., Yu, L. S., and Tziperman, E.: Westerly wind bursts: ENSO's tail rather than the dog?, J. Climate, 18, 5224–5237, https://doi.org/10.1175/JCLI3588.1, 2005.

Eyring, V., Bony, S., Meehl, G. A., Senior, C. A., Stevens, B., Stouffer, R. J., and Taylor, K. E.: Overview of the Coupled Model Intercomparison Project Phase 6 (CMIP6) experimental design and organization, Geosci. Model Dev., 9, 1937–1958, https://doi.org/10.5194/gmd-9-1937-2016, 2016.

Fedorov, A. V.: The response of the coupled tropical ocean–atmosphere to westerly wind bursts, Q. J. Roy. Meteorol. Soc., 128, 1–23, https://doi.org/10.1002/qj.200212857901, 2002.

Fedorov, A. V., Hu, S. N., Lengaigne, M., and Guilyardi, E.: The impact of westerly wind bursts and ocean initial state on the development, and diversity of El Niño events, Clim. Dynam., 44, 1381–1401, https://doi.org/10.1007/s00382-014-2126-4, 2015.

Gebbie, G. and Tziperman, E.: Incorporating a semi-stochastic model of ocean-modulated westerly wind bursts into an ENSO prediction model, Theor. Appl. Climatol., 97, 65–73, https://doi.org/10.1007/s00704-008-0069-6, 2009.

Gebbie, G., Eisenman, I., Wittenberg, A., and Tziperman, E.: Modulation of westerly wind bursts by sea surface temperature: A semistochastic feedback for ENSO, J. Atmos. Sci., 64, 3281–3295, https://doi.org/10.1175/jas4029.1, 2007.

Griffies, S. M., Danabasoglu, G., Durack, P. J., Adcroft, A. J., Balaji, V., Böning, C. W., Chassignet, E. P., Curchitser, E., Deshayes, J., Drange, H., Fox-Kemper, B., Gleckler, P. J., Gregory, J. M., Haak, H., Hallberg, R. W., Heimbach, P., Hewitt, H. T., Holland, D. M., Ilyina, T., Jungclaus, J. H., Komuro, Y., Krasting, J. P., Large, W. G., Marsland, S. J., Masina, S., McDougall, T. J., Nurser, A. J. G., Orr, J. C., Pirani, A., Qiao, F., Stouffer, R. J., Taylor, K. E., Treguier, A. M., Tsujino, H., Uotila, P., Valdivieso, M., Wang, Q., Winton, M., and Yeager, S. G.: OMIP contribution to CMIP6: experimental and diagnostic protocol for the physical component of the Ocean Model Intercomparison Project, Geosci. Model Dev., 9, 3231–3296, https://doi.org/10.5194/gmd-9-3231-2016, 2016.

Guilyardi, E., Gualdi, S., Slingo, J., Navarra, A., Delecluse, P., Cole, J., Madec, G., Roberts, M., Latif, M., and Terray, L.: Representing El Niño in coupled ocean–atmosphere GCMs: The dominant role of the atmospheric component, J. Climate, 17, 4623–4629, https://doi.org/10.1175/JCLI-3260.1, 2004.

Guilyardi, E., Capotondi, A., Lengaigne, M., Thual, S., and Wittenberg, A. T.: ENSO modeling: History, progress, and challenges, in: El Niño Southern Oscillation in a Changing Climate, edited by: McPhaden, M. J., Santoso, A., and Cai, W., American Geophysical Union, American, 199–226, https://doi.org/10.1002/9781119548164.ch9, 2020.

Hallberg, R.: Using a resolution function to regulate parameterizations of oceanic mesoscale eddy effects, Ocean Model., 72, 92–103, https://doi.org/10.1016/j.ocemod.2013.08.007, 2013.

Harrison, D. E. and Vecchi, G. A.: Westerly wind events in the tropical Pacific, 1986–95, J. Climate, 10, 3131–3156, https://doi.org/10.1175/1520-0442(1997)010<3131:Wweitt>2.0.Co;2, 1997.

He, B., Bao, Q., Wang, X. C., Zhou, L. J., Wu, X. F., Liu, Y. M., Wu, G. X., Chen, K. J., He, S. C., Hu, W. T., Li, J. D., Li, J. X., Nian, G. K., Wang, L., Yang, J., Zhang, M. H., and Zhang, X. Q.: CAS

FGOALS-f3-L model datasets for CMIP6 historical atmospheric model intercomparison project simulation, Adv. Atmos. Sci., 36, 771–778, https://doi.org/10.1007/s00376-019-9027-8, 2019.

He, B., He, X. Y., Liu, Y. M., Wu, G. X., Bao, Q., Hu, W. T., Sheng, C., and Feng, S. J.: Role of thermal and dynamical subdaily perturbations over the Tibetan Plateau in 30-day extended-range forecast of East Asian precipitation in early summer, npj Clim. Atmos. Sci., 8, https://doi.org/10.1038/s41612-025-00931-2, 2025a.

He, X.-Y., He, B., Bao, Q., Liu, Y.-M., Li, J.-D., Wang, X.-C., Chen, X.-C., and Wu, G.-X.: The sensitivity of the Asian summer monsoon simulation to horizontal resolution and airsea coupling in the FGOALS-f climate system model, Adv. Clim. Change Res., 16, 44–57, https://doi.org/10.1016/j.accre.2025.01.008, 2025b.

Hersbach, H., Bell, B., Berrisford, P., Hirahara, S., Horányi, A., Muñoz-Sabater, J., Nicolas, J., Peubey, C., Radu, R., Schepers, D., Simmons, A., Soci, C., Abdalla, S., Abellan, X., Balsamo, G., Bechtold, P., Biavati, G., Bidlot, J., Bonavita, M., De Chiara, G., Dahlgren, P., Dee, D., Diamantakis, M., Dragani, R., Flemming, J., Forbes, R., Fuentes, M., Geer, A., Haimberger, L., Healy, S., Hogan, R. J., Hólm, E., Janisková, M., Keeley, S., Laloyaux, P., Lopez, P., Lupu, C., Radnoti, G., de Rosnay, P., Rozum, I., Vamborg, F., Villaume, S., and Thépaut, J. N.: The ERA5 global reanalysis, Q. J. Roy. Meteorol. Soc., 146, 1999–2049, https://doi.org/10.1002/qj.3803, 2020.

Hewitt, H. T., Roberts, M. J., Hyder, P., Graham, T., Rae, J., Belcher, S. E., Bourdallé-Badie, R., Copsey, D., Coward, A., Guiavarch, C., Harris, C., Hill, R., Hirschi, J. J.-M., Madec, G., Mizielinski, M. S., Neininger, E., New, A. L., Rioual, J.-C., Sinha, B., Storkey, D., Shelly, A., Thorpe, L., and Wood, R. A.: The impact of resolving the Rossby radius at mid-latitudes in the ocean: results from a high-resolution version of the Met Office GC2 coupled model, Geosci. Model Dev., 9, 3655–3670, https://doi.org/10.5194/gmd-9-3655-2016, 2016.

Hua, L. J., Chen, L., Rong, X. Y., Su, J. Z., Wang, L., Li, T., and Yu, Y. Q.: Impact of atmospheric model resolution on simulation of ENSO feedback processes: a coupled model study, Clim. Dynam., 51, 3077–3092, https://doi.org/10.1007/s00382-017-4066-2, 2018.

Hunke, E. C. and Lipscomb, W. H.: CICE: The Los Alamos Sea Ice Model, Documentation and Software User's Manual, Version 4.1, Tech. Rep. LA-CC-06-012, Los Alamos National Laboratory, Los Alamos, New Mexico, https://www.icams-portal.gov/resources/espc/esps/sea_ice_models.html (last access: 28 May 2026), 2010.

Jiang, W. P., Huang, P., Li, G., and Huang, G.: Emergent constraint on the frequency of central Pacific El Niño under global warming by the equatorial Pacific cold tongue bias in CMIP5/6 models, Geophys. Res. Lett., 47, https://doi.org/10.1029/2020gl089519, 2020a.

Jiang, W. P., Huang, P., Huang, G., and Ying, J.: Origins of the excessive westward extension of ENSO SST simulated in CMIP5 and CMIP6 models, J. Climate, 34, 2839–2851, https://doi.org/10.1175/jcli-d-20-0551.1, 2021.

Jiang, X. N., Adames, Á. F., Kim, D., Maloney, E. D., Lin, H., Kim, H., Zhang, C. D., DeMott, C. A., and Klingaman, N. P.: Fifty years of research on the Madden-Julian Oscillation: Recent progress, challenges, and perspectives, J. Geophys. Res.-Atmos., 125, https://doi.org/10.1029/2019jd030911, 2020b.

Jin, F.-F.: An equatorial ocean recharge paradigm for ENSO. Part I: Conceptual model, J. Atmos. Sci., 54, 811–829, https://doi.org/10.1175/1520-0469(1997)054<0811:Aeorpf>2.0.Co;2, 1997.

Jin, F. F., Kim, S. T., and Bejarano, L.: A coupled-stability index for ENSO, Geophys. Res. Lett., 33, https://doi.org/10.1029/2006gl027221, 2006.

Kim, S. T. and Jin, F.-F.: An ENSO stability analysis. Part II: Results from the twentieth and twenty-first century simulations of the CMIP3 models, Clim. Dynam., 36, 1609–1627, https://doi.org/10.1007/s00382-010-0872-5, 2011a.

Kim, S. T. and Jin, F.-F.: An ENSO stability analysis. Part I: results from a hybrid coupled model, Clim. Dynam., 36, 1593–1607, https://doi.org/10.1007/s00382-010-0796-0, 2011b.

Kreussler, P., Caron, L. P., Wild, S., Loosveldt Tomas, S., Chauvin, F., Moine, M. P., Roberts, M. J., Ruprich-Robert, Y., Seddon, J., Valcke, S., Vannière, B., and Vidale, P. L.: Tropical cyclone integrated kinetic energy in an ensemble of HighResMIP simulations, Geophys. Res. Lett., 48, https://doi.org/10.1029/2020gl090963, 2021.

Lawrence, D. M., Oleson, K. W., Flanner, M. G., Thornton, P. E., Swenson, S. C., Lawrence, P. J., Zeng, X., Yang, Z. L., Levis, S., and Sakaguchi, K.: Parameterization improvements and functional and structural advances in version 4 of the Community Land Model, J. Adv. Model. Earth Syst., 3, https://doi.org/10.1029/2011MS00045, 2011.

Li, J., Bao, Q., Liu, Y., Wang, L., Yang, J., Wu, G., Wu, X., He, B., Wang, X., Zhang, X., Yang, Y., and Shen, Z.: Effect of horizontal resolution on the simulation of tropical cyclones in the Chinese Academy of Sciences FGOALS-f3 climate system model, Geosci. Model Dev., 14, 6113–6133, https://doi.org/10.5194/gmd-14-6113-2021, 2021.

Li, J., Yu, Y. Q., and Sun, D. Z.: Asymmetric Responses in the Equatorial Pacific to Wind Forcing in OMIP2 Experiments: Role of Zonal Currents, Geophys. Res. Lett., 52, e2025GL114661, https://doi.org/10.1029/2025gl114661, 2025.

Li, T.: Phase transition of the El Niño–Southern Oscillation: A stationary SST mode, J. Atmos. Sci., 54, 2872–2887, https://doi.org/10.1175/1520-0469(1997)054<2872:PTOTEN>2.0.CO;2, 1997.

Li, T. Y., Yu, Y. Q., An, B., Luan, Y. H., and Chen, K. J.: Tropical instability waves in a high-resolution oceanic and coupled GCM, Ocean Model., 182, https://doi.org/10.1016/j.ocemod.2023.102169, 2023.

Li, Y., Liu, H., Ding, M., Lin, P., Yu, Z., Yu, Y., Meng, Y., Li, Y., Jian, X., and Jiang, J.: Eddy-resolving simulation of CAS-LICOM3 for phase 2 of the ocean model intercomparison project, Adv. Atmos. Sci., 37, 1067–1080, https://doi.org/10.1007/s00376-020-0057-z, 2020.

Liang, Y. and Fedorov, A. V.: Linking the Madden–Julian Oscillation, tropical cyclones and westerly wind bursts as part of El Niño development, Clim. Dynam., 57, 1039–1060, https://doi.org/10.1007/s00382-021-05757-1, 2021.

Liao, H. X., Cai, Z. C., Guo, J. S., and Song, Z. Y.: Effects of ITCZ poleward location bias on ENSO seasonal phase-locking simulation in climate models, J. Climate, 36, 5233–5249, https://doi.org/10.1175/jcli-d-22-0891.1, 2023.

Lu, B., Jin, F.-F., and Ren, H.-L.: A coupled dynamic index for ENSO periodicity, J. Climate, 31, 2361–2376, https://doi.org/10.1175/jcli-d-17-0466.1, 2018.

Lu, X. Q., Yu, H., Ying, M., Zhao, B. K., Zhang, S., Lin, L. M., Bai, L. N., and Wan, R. J.: Western north Pacific tropical cyclone database created by the China Meteorological Administration, Adv. Atmos. Sci., 38, 690–699, https://doi.org/10.1007/s00376-020-0211-7, 2021.

Ma, T., Yu, W.-D., Speich, S., Zhao, H.-K., Xin, R., Luo, H., and Wu, L.-G.: Philippine archipelago and South China Sea monsoon plus ocean cooling buffer Northwestern Pacific super typhoons, Nat. Commun., 16, https://doi.org/10.1038/s41467-025-62334-4, 2025.

Madden, R. A. and Julian, P. R.: Detection of a 40–50 day oscillation in the zonal wind in the tropical Pacific, J. Atmos. Sci., 28, 702–708, https://doi.org/10.1175/1520-0469(1971)028<0702:DOADOI>2.0.CO;2, 1971.

Madden, R. A. and Julian, P. R.: Description of global-scale circulation cells in the tropics with a 40–50 day period, J. Atmos. Sci., 29, 1109–1123, https://doi.org/10.1175/1520-0469(1972)029<1109:DOGSCC>2.0.CO;2, 1972.

McPhaden, M. J., Zebiak, S. E., and Glantz, M. H.: ENSO as an integrating concept in earth science, Science, 314, 1740–1745, https://doi.org/10.1126/science.1132588, 2006.

Moore, A. M. and Kleeman, R.: Stochastic forcing of ENSO by the intraseasonal oscillation, J. Climate, 12, 1199–1220, https://doi.org/10.1175/1520-0442(1999)012<1199:Sfoebt>2.0.Co;2, 1999.

Nakamura, J., Camargo, S. J., Sobel, A. H., Henderson, N., Emanuel, K. A., Kumar, A., LaRow, T. E., Murakami, H., Roberts, M. J., Scoccimarro, E., Vidale, P. L., Wang, H., Wehner, M. F., and Zhao, M.: Western North Pacific Tropical Cyclone Model Tracks in Present and Future Climates, J. Geophys. Res.-Atmos., 122, 9721–9744, https://doi.org/10.1002/2017jd027007, 2017.

Navarra, A., Gualdi, S., Masina, S., Behera, S., Luo, J. J., Masson, S., Guilyardi, E., Delecluse, P., and Yamagata, T.: Atmospheric horizontal resolution affects tropical climate variability in coupled models, J. Climate, 21, 730–750, https://doi.org/10.1175/2007jcli1406.1, 2008.

Planton, Y. Y., Guilyardi, E., Wittenberg, A. T., Lee, J., Gleckler, P. J., Bayr, T., McGregor, S., McPhaden, M. J., Power, S., Roehrig, R., Vialard, J., and Voldoire, A.: Evaluating climate models with the CLIVAR 2020 ENSO metrics package, B. Am. Meteorol. Soc., 102, E193–E217, https://doi.org/10.1175/bams-d-19-0337.1, 2021.

Rayner, N. A., Parker, D. E., Horton, E. B., Folland, C. K., Alexander, L. V., Rowell, D. P., Kent, E. C., and Kaplan, A.: Global analyses of sea surface temperature, sea ice, and night marine air temperature since the late nineteenth century, J. Geophys. Res.-Atmos., 108, https://doi.org/10.1029/2002jd002670, 2003.

Roberts, M. J., Camp, J., Seddon, J., Vidale, P. L., Hodges, K., Vanniere, B., Mecking, J., Haarsma, R., Bellucci, A., Scoccimarro, E., Caron, L.-P., Chauvin, F., Terray, L., Valcke, S., Moine, M.-P., Putrasahan, D., Roberts, C., Senan, R., Zarzycki, C., and Ullrich, P.: Impact of model resolution on tropical cyclone simulation using the HighResMIP–PRIMAVERA multimodel ensemble, J. Climate, 33, 2557–2583, https://doi.org/10.1175/jcli-d-19-0639.1, 2020a.

Roberts, M. J., Camp, J., Seddon, J., Vidale, P. L., Hodges, K., Vannière, B., Mecking, J., Haarsma, R., Bellucci, A., Scoccimarro, E., Caron, L. P., Chauvin, F., Terray, L., Valcke, S., Moine, M. P., Putrasahan, D., Roberts, C. D., Senan, R., Zarzycki, C., Ullrich, P., Yamada, Y., Mizuta, R., Kodama, C., Fu, D., Zhang, Q., Danabasoglu, G., Rosenbloom, N., Wang, H., and Wu, L.: Projected future changes in tropical cyclones using the CMIP6 HighResMIP multimodel ensemble, Geophys. Res. Lett., 47, e2020GL088662, https://doi.org/10.1029/2020gl088662, 2020b.

Roberts, M. J., Reed, K. A., Bao, Q., Barsugli, J. J., Camargo, S. J., Caron, L.-P., Chang, P., Chen, C.-T., Christensen, H. M., Danabasoglu, G., Frenger, I., Fučkar, N. S., ul Hasson, S., Hewitt, H. T., Huang, H., Kim, D., Kodama, C., Lai, M., Leung, L.-Y. R., Mizuta, R., Nobre, P., Ortega, P., Paquin, D., Roberts, C. D., Scoccimarro, E., Seddon, J., Treguier, A. M., Tu, C.-Y., Ullrich, P. A., Vidale, P. L., Wehner, M. F., Zarzycki, C. M., Zhang, B., Zhang, W., and Zhao, M.: High-Resolution Model Intercomparison Project phase 2 (HighResMIP2) towards CMIP7, Geosci. Model Dev., 18, 1307–1332, https://doi.org/10.5194/gmd-18-1307-2025, 2025.

Rong, X. Y., Zhang, R. H., Li, T., and Su, J. Z.: Upscale feedback of high-frequency winds to ENSO, Q. J. Roy. Meteorol. Soc., 137, 894–907, https://doi.org/10.1002/qj.804, 2011.

Savarin, A. and Chen, S. S.: Pathways to better prediction of the MJO: 1. Effects of model resolution and moist physics on Atmospheric boundary layer and precipitation, J. Adv. Model. Earth Syst., 14, e2021MS002928, https://doi.org/10.1029/2021ms002929, 2022.

Small, R. J., Bryan, F. O., Bishop, S. P., and Tomas, R. A.: Air–Sea turbulent heat fluxes in climate models and observational analyses: What drives their variability?, J. Climate, 32, 2397–2421, https://doi.org/10.1175/jcli-d-18-0576.1, 2019.

Song, M.-E., Chen, L., Yu, Y. Q., An, B., Zhao, J., and Zhi, H.: Source code and analysis data for "Process-based evaluation of ENSO simulation sensitivity to horizontal resolution in the Chinese Academy of Sciences FGOALS-f3 Climate System Model", Zenodo [code], https://doi.org/10.5281/zenodo.19552337, 2026.

Su, J. Z., Zhang, R. H., Li, T., Rong, X. Y., Kug, J. S., and Hong, C.-C.: Causes of the El Niño and La Niña amplitude asymmetry in the equatorial eastern Pacific, J. Climate, 23, 605–617, https://doi.org/10.1175/2009jcli2894.1, 2010.

Su, J. Z., Li, T., and Zhang, R. H.: The initiation and developing mechanisms of central Pacific El Niños, J. Climate, 27, 4473–4485, https://doi.org/10.1175/jcli-d-13-00640.1, 2014.

Sun, M., Li, T. and Chen, L.: El Niño phase-dependent high-frequency variability in western equatorial Pacific, Clim. Dynam., 55, 2165–2184, https://doi.org/10.1007/s00382-020-05376-2, 2020.

Tang, Y. L., HuangFu, J. l., Huang, R. H., and Chen, W.: Simulation and projection of tropical cyclone activities over the western North Pacific by CMIP6 HighResMIP, Clim. Dynam., 35, 7771–7794, https://doi.org/10.1175/JCLI-D-21-0760.1, 2022.

Thomson, D. J.: Spectrum estimation and harmonic analysis, Proc. IEEE, 79, 1055–1096, https://doi.org/10.1109/PROC.1982.12433, 1982.

Timmermann, A., An, S. I., Kug, J. S., Jin, F. F., Cai, W., Capotondi, A., Cobb, K. M., Lengaigne, M., McPhaden, M. J., Stuecker, M. F., Stein, K., Wittenberg, A. T., Yun, K. S., Bayr, T., Chen, H. C., Chikamoto, Y., Dewitte, B., Dommenget, D., Grothe,

P., Guilyardi, E., Ham, Y. G., Hayashi, M., Ineson, S., Kang, D., Kim, S., Kim, W., Lee, J. Y., Li, T., Luo, J. J., McGregor, S., Planton, Y., Power, S., Rashid, H., Ren, H. L., Santoso, A., Takahashi, K., Todd, A., Wang, G., Wang, G., Xie, R., Yang, W. H., Yeh, S. W., Yoon, J., Zeller, E., and Zhang, X.: El Nino-Southern Oscillation complexity, Nature, 559, 535–545, https://doi.org/10.1038/s41586-018-0252-6, 2018.

Wang, L., Li, T., and Zhou, T. J.: Intraseasonal SST variability and air–sea interaction over the Kuroshio extension region during boreal summer, J. Climate, 25, 1619–1634, https://doi.org/10.1175/JCLI-D-11-00109.1, 2012.

Wei, X. J., Chen, L. and Sun, M.: Fine-tuning Atmospheric Parameters for Improving ENSO Simulation in the Zebiak–Cane Model, Adv. Atmos. Sci., 43, 420–435, https://doi.org/10.1007/s00376-025-4423-8, 2026.

Yan, Y. and Sun, D.-Z.: Phase-Locking of El Niño and La Niña events in CMIP6 models, Atmosphere, 15, 882, https://doi.org/10.3390/atmos15080882, 2024.

Ying, J., Lian, T., Ren, H.-L., Zhang, C., Liu, T., and Tan, X.-X.: Effects of tropical cyclones on ENSO, J. Climate, 32, 6423–6443, https://doi.org/10.1175/jcli-d-18-0821.1, 2019.

Ying, M., Zhang, W., Yu, H., Lu, X. Q., Feng, J. X., Fan, Y. X., Zhu, Y. T., and Chen, D. Q.: An overview of the China Meteorological Administration tropical cyclone database, J. Atmos. Ocean. Tech., 31, 287–301, https://doi.org/10.1175/JTECH-D-12-00119.1, 2014.

Yu, Y. Q., Tang, S. L., Liu, H. L., Lin, P. F., and Li, X. L.: Development and evaluation of the dynamic framework of an ocean general circulation model with arbitrary orthogonal curvilinear coordinate, Chinese J. Atmos. Sci., 42, 877–889, https://doi.org/10.3878/j.issn.1006-9895.1805.17284, 2018.

Yu, Y. Q., An, B., Liu, H. L., Bao, Q., Lin, P. F., He, B., Zheng, W. P., Luan, Y. H., Bai, R., and Li, T. Y.: Review of the development and application of the high-resolution climate system model FGOALS, Chinese J. Atmos. Sci., 48, 200–217, https://doi.org/10.1007/BF02915571, 2024.

Zhang, R.-H., Yu, Y. Q., Song, Z. Y., Ren, H.-L., Tang, Y. M., Qiao, F. L., Wu, T. W., Gao, C., Hu, J. Y., Tian, F., Zhu, Y. C., Chen, L., Liu, H. L., Lin, P. F., Wu, F. H., and Wang, L.: A review of progress in coupled ocean-atmosphere model developments for ENSO studies in China, J. Oceanol. Limnol., 38, 930–961, https://doi.org/10.1007/s00343-020-0157-8, 2020.

Zhao, J. W., Wang, F., Zhan, R. F., Guo, Y. P., Huang, X., and Liu, C.: How Does Tropical Cyclone Genesis Frequency Respond to a Changing Climate?, Geophys. Res. Lett., 50, https://doi.org/10.1029/2023gl102879, 2023.

Zhao, Y. D. and Sun, D.-Z.: ENSO asymmetry in CMIP6 models, J. Climate, 35, 5555–5572, https://doi.org/10.1175/jcli-d-21-0835.1, 2022.

Zhou, L., Bao, Q., Liu, Y. M., Wu, G. X., Wang, W. C., Wang, X. C., He, B., Yu, H. Y., and Li, J. D.: Global energy and water balance: Characteristics from Finite-volume Atmospheric Model of the IAP/LASG (FAMIL 1), J. Adv. Model. Earth Syst., 7, 1–20, https://doi.org/10.1002/2014MS000349, 2015.

Zi, P., Liu, Y. M., Li, J. D., Yang, R. W., He, B., and Bao, Q.: Reduced Spring Precipitation Bias and Associated Physical Causes over South China in FGOALS-f3 Climate Models: Experiments with the Horizontal Resolutions, J. Meteorol. Res.-PRC, 38, 784–804, https://doi.org/10.1007/s13351-024-3200-4, 2024.

Zuo, H., Balmaseda, M. A., Tietsche, S., Mogensen, K., and Mayer, M.: The ECMWF operational ensemble reanalysis–analysis system for ocean and sea ice: a description of the system and assessment, Ocean Sci., 15, 779–808, https://doi.org/10.5194/os-15-779-2019, 2019.